



This is a repository copy of *Constant slip-rate on the Doruneh strike-slip fault, Iran, averaged over Late Pleistocene, Holocene, and decadal timescales.*

White Rose Research Online URL for this paper:  
<https://eprints.whiterose.ac.uk/173395/>

Version: Published Version

---

**Article:**

Mousavi, Z., Fattahi, M., Khatib, M. et al. (9 more authors) (2021) Constant slip-rate on the Doruneh strike-slip fault, Iran, averaged over Late Pleistocene, Holocene, and decadal timescales. *Tectonics*, 40 (6). e2020TC006256. ISSN 0278-7407

<https://doi.org/10.1029/2020tc006256>

---

**Reuse**

This article is distributed under the terms of the Creative Commons Attribution (CC BY) licence. This licence allows you to distribute, remix, tweak, and build upon the work, even commercially, as long as you credit the authors for the original work. More information and the full terms of the licence here:  
<https://creativecommons.org/licenses/>

**Takedown**

If you consider content in White Rose Research Online to be in breach of UK law, please notify us by emailing [eprints@whiterose.ac.uk](mailto:eprints@whiterose.ac.uk) including the URL of the record and the reason for the withdrawal request.



[eprints@whiterose.ac.uk](mailto:eprints@whiterose.ac.uk)  
<https://eprints.whiterose.ac.uk/>

# Tectonics

## RESEARCH ARTICLE

10.1029/2020TC006256

### Key Points:

- We compare present-day strain accumulation and late Quaternary slip on the Doruneh fault, Iran
- We conclude that the fault has slipped at a constant rate of  $2.5 \pm 0.3$  mm/yr throughout the last ~100 ka

### Correspondence to:

R. T. Walker,  
richard.walker@earth.ox.ac.uk

### Citation:

Mousavi, Z., Fattahi, M., Khatib, M., Talebian, M., Pathier, E., Walpersdorf, A., et al. (2021). Constant slip rate on the Doruneh strike-slip fault, Iran, averaged over late Pleistocene, Holocene, and decadal timescales. *Tectonics*, 40, e2020TC006256. <https://doi.org/10.1029/2020TC006256>

Received 2 MAY 2020  
Accepted 11 FEB 2021

© Wiley Periodicals LLC. The Authors. This is an open access article under the terms of the [Creative Commons Attribution License](#), which permits use, distribution and reproduction in any medium, provided the original work is properly cited.

# Constant Slip Rate on the Doruneh Strike-Slip Fault, Iran, Averaged Over Late Pleistocene, Holocene, and Decadal Timescales

Zahra Mousavi<sup>1</sup> , Morteza Fattahi<sup>2</sup>, Mohammad Khatib<sup>3</sup>, Morteza Talebian<sup>4</sup> , Erwan Pathier<sup>5</sup> , Andrea Walpersdorf<sup>5</sup> , R. Alastair Sloan<sup>6</sup> , Alexander L. Thomas<sup>7</sup>, Ed Rhodes<sup>8</sup> , Fynn Clive<sup>9,10</sup> , Nicholas Dodds<sup>9</sup>, and Richard T. Walker<sup>9</sup> 

<sup>1</sup>Department of Earth Sciences, Institute for Advanced Studies in Basic Sciences, Zanjan, Iran, <sup>2</sup>Institute of Geophysics, University of Tehran, Tehran, Iran, <sup>3</sup>Department of Geology, University of Birjand, Birjand, Iran, <sup>4</sup>Research Institute for Earth Sciences, Geological Survey of Iran, Azadi Square, Tehran, Iran, <sup>5</sup>ISterre, Université Joseph Fourier, CNRS UMR 5275, Grenoble, France, <sup>6</sup>Department of Geological Sciences, University of Cape Town, Rondebosch, South Africa, <sup>7</sup>School of Geosciences, University of Edinburgh, Edinburgh, UK, <sup>8</sup>Department of Geography, University of Sheffield, Sheffield, UK, <sup>9</sup>Department of Earth Sciences, University of Oxford, Oxford, UK, <sup>10</sup>Now at Shell International Exploration and Production, The Hague, The Netherlands

**Abstract** Varying estimates of both present-day strain accumulation and long-term slip rate on the Doruneh left-lateral strike-slip fault, NE Iran, have led to suggestions that it exhibits large along-strike and/or temporal changes in activity. In this study, we make and compare estimates of slip rate measured using both geodesy and geomorphology, and spanning time periods ranging from decadal to 100 ka. To image the present-day accumulation of strain, we process 7 years (2003–2010) of data from six ENVISAT tracks covering the fault, with interferograms produced for 400-km-long strips of data to image the long-wavelength signals associated with interseismic strain accumulation across the locked fault. Our analysis shows that less than 4 mm/yr—and likely only 1–3 mm/yr—of slip accumulates across the fault. Using high-resolution optical satellite imagery, we make reconstructions of displacement across six alluvial fans whose surfaces cross the fault, in four separate river catchments. We determine the ages of these fans using infra-red-stimulated luminescence dating combined with U-series dating of pedogenic carbonates. The six fans vary in age from ~10– to 100 kyr, and a regression line fitted to four of these yields a slip rate of  $2.5 \pm 0.3$  mm/yr. We conclude that within the uncertainty of our measurements, the slip rate has remained constant over the last ~100 ka and is representative of the strain accumulation at the present-day. The slip rate that we measure is consistent with the E-W left-lateral Doruneh fault accommodating N-S right-lateral faulting by “bookshelf” faulting, with clockwise rotation about a vertical axis.

## 1. Introduction

The last 15 years have seen a rapid increase in the number and distribution of GPS and InSAR measurements of tectonic strain across Iran (e.g., Djamour et al., 2011; Mousavi et al., 2013; Mousavi et al., 2015; Tavakoli et al., 2008; Vernant et al., 2004; Walpersdorf et al., 2006, 2014), and also of the Holocene and late Pleistocene slip rates on many of its major active faults (e.g., Fattahi & Walker, 2006; Fattahi et al., 2014; Foroutan et al., 2014; Regard et al., 2005; Ritz et al., 2003; Rizza et al., 2011; Talebian et al., 2016). These complementary sets of data offer insight into the ongoing debate over the extent to which late Quaternary slip rates on major active faults are representative of the present-day accumulation of tectonic strain across them.

There is broad agreement between the geodetic strain accumulation and the long-term average slip rate in most of those places where meaningful comparisons can be made (e.g., Mousavi et al., 2013; Rizza et al., 2013; Walker et al., 2010; Walpersdorf et al., 2014). However, variations in slip rate have been suggested for a small number of the active strike-slip faults in north-eastern Iran, potentially suggesting that the long-term fault behavior in that region is fundamentally different from in other parts of the orogen (e.g., Farbod et al., 2011, 2016; Shabaniyan et al., 2009). If real, these variations have the potential to yield insights into the mechanical behavior of fault zones and of the continental crust. The presence of time-varying fault slip rates also has implications for estimates of seismic hazard, as they imply that measurements of

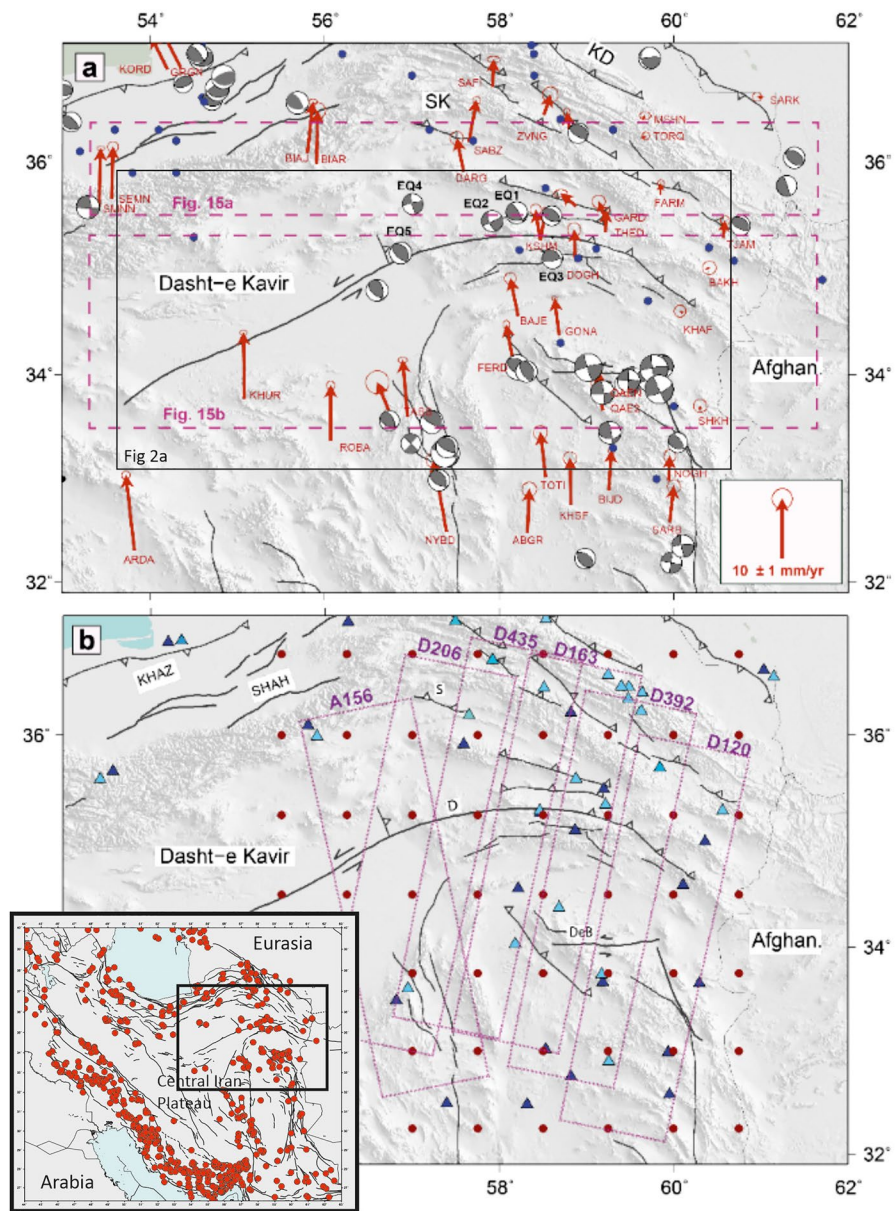


**Figure 1.** Shaded relief topography of NE Iran. (a) GPS velocity field (Mousavi et al., 2013; Walpersdorf et al. 2014) and focal mechanisms of earthquakes, including both first-motion and waveform-modeled solutions from McKenzie (1972), Baker et al. (1993), and Walker and Jackson (2004) and the Global CMT catalog (<http://www.globalcmt.org/CMTsearch.html>) during the period 1976–2012. Epicenters of these earthquakes are from Engdahl et al. (2006). Historical earthquakes (blue dots) come from Ambraseys and Melville (1982). (b) Shows the spatial coverage of the ENVISAT SAR tracks across the Doruneh fault. We used the ERA\_Interim model, (the red dots) to correct the tropospheric delay and we used both the permanent and campaign GPS stations to validate the tropospheric delay map. The inset shows the region represented in “a” and “b” within the overall Arabia-Eurasia collision as a black box, with earthquakes from Engdahl et al. (1998). SAR, synthetic aperture radar.

long-term fault slip rate (i.e., those averaged over many earthquake cycles) are not necessarily representative of the accumulation of strain at the present day.

Our focus in the present study is the Doruneh strike-slip fault of NE Iran (Figure 1), which has been suggested to display significant variability in slip rate through time (Farbod et al., 2011, 2016; Pezzo et al., 2012). The Doruneh fault is one of the major strike-slip faults in Iran, extending for 700 km from the eastern border of Iran to the central Dasht-e-Kavir (Berberian, 1976; Farbod et al., 2011, 2016; Fattahi et al., 2007;

Jackson & McKenzie, 1984; Pezzo et al., 2012; Walker & Jackson, 2004; Wellman, 1966). It is prominent in geomorphology and displays numerous indications of cumulative left-lateral displacements (Tchalenko et al., 1973; Farbod et al., 2011, 2016; Fattahi et al., 2007; Wellman, 1966).

Geodetic measurements of interseismic strain accumulation across the Doruneh fault are contradictory: Pezzo et al. (2012) measure  $\sim 5$  mm/yr of left-lateral strain accumulation from synthetic aperture radar (SAR) interferometry, whereas campaign and permanent GPS measurements (Mousavi et al., 2013; Walpersdorf et al., 2014), show little discernible strain accumulation, with a maximum  $\sim 2$  mm/yr. Late Quaternary estimates of left-lateral slip rate range from  $\sim 2.5$  to  $3.0$  mm/yr (Fattahi et al., 2007; Walker & Fattahi, 2011), up to  $> 8$  mm/yr, with  $\sim 5.3$  mm/yr in the Holocene, in the study presented by Farbod et al. (2011, 2016).

Here, we assess the slip on the Doruneh fault averaged over timescales ranging from 10 years to 100,000 years. In Section 4, we provide a study of interseismic strain accumulation along the entire fault length using InSAR. In Section 5, we present ages for alluvial fans that have been displaced by the Doruneh fault and carefully reassess previous interpretations of the geomorphology of each site. The ages allow us to make six separate estimates of slip rate, averaged over time periods ranging from 100 to 10 ka, and from sites spanning a distance of  $\sim 40$  km in the central part of the Doruneh fault, coincident with where high ( $> 8$  mm/yr) slip rates were postulated by Farbod et al. (2011, 2016). Finally, in Section 6, we discuss the implications of our slip rates in assessing the differing ideas for the role of the Doruneh fault in accommodating regional tectonic motions.

## 2. Tectonic Setting

The active tectonics of Iran result from the continental collision of Arabia and Eurasia (Figure 1, inset). GPS velocities indicate  $\sim 30$  mm/yr of northward-directed shortening relative to Eurasia at longitude  $54^\circ\text{E}$ . Almost half of this shortening is accommodated within the Zagros Mountains, with most of the remainder accommodated within the Alborz Mountains of northern Iran. The Central Iranian Plateau has few earthquakes recorded within it, and is likely to be deforming at much slower rates than its surroundings. The GPS velocity field shows that northward directed shortening relative to Eurasia decreases from  $\sim 15$  mm/yr within the central Iranian plateau to close to zero near the Afghan border (Figure 1). This N-S right-lateral shear is accommodated south of latitude  $34^\circ\text{N}$  by a series of N-S right-lateral strike-slip faults within eastern Iran. North of  $34^\circ\text{N}$ , the GPS velocities in NE Iran show the same N-S right-lateral shear as they do further south, and yet the dominant active structures are E-W left-lateral faults, including the Dasht-e-Bayaz and Doruneh faults. These E-W left-lateral faults, and the regions between them, can accommodate the N-S right-lateral shear indicated by GPS measurements if they rotate clockwise about a vertical axis, as confirmed by recent paleomagnetic measurements in NE Iran (Mattei et al., 2017). Others have argued that the Doruneh fault allows a westward expulsion in the region north of it (e.g., Farbod et al., 2011, 2016); however, this model is not supported by the GPS velocities.

Although being one of the longest and most prominent active faults in Iran, there are few large earthquakes associated with it (e.g., Figure 2a). Destructive events occurred along the Doruneh fault in 1903 and 1926, with the first of these causing damage in a zone westwards from Kashmar, and the second southwest of Torbat Heydarieh (Figure 2a; Fattahi et al., 2007). The damage from both of these earthquakes was quite limited in extent. There are no records of major earthquakes on the Doruneh fault further back in history. Fattahi et al. (2007) report a number of streams offset by 3–5.5 m along the central section of the fault, which they suggest result from displacement in a single earthquake of magnitude  $\sim 7.5$ .

## 3. Methods

Our study combines analysis of satellite RADAR, optical satellite imagery interpretation, field-based geological sampling, and analytical dating. The InSAR methods are described in full in the text of Section 4. The optical image analysis is based on 50-cm Quickbird satellite data from 2003, which predates the quarrying that has since destroyed much of the geomorphology of Site 1. Best-fitting measurements of strike-slip displacement are made visually by realignment of the channel thalwegs, with an uncertainty centered on these best-fitting measurements estimated from realignment of the thalweg on the upstream side of the fault with

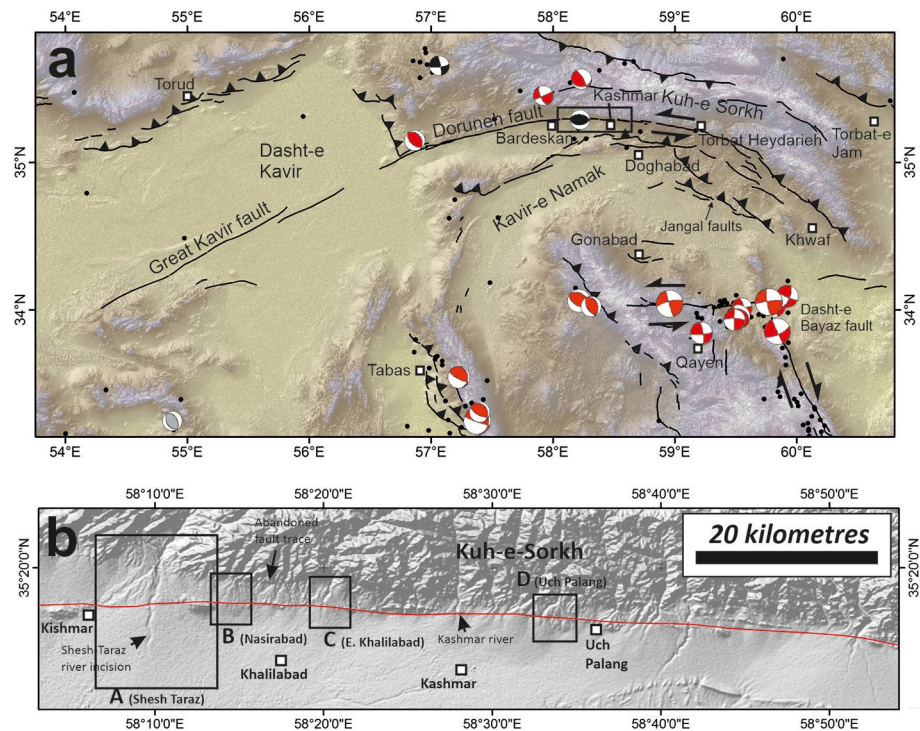


**Figure 2.** (a) Shaded-relief SRTM topographic map of the region around the Doruneh fault (see Green box in Figure 1a for location). Major faults are marked, along with the focal mechanisms of earthquakes. (b) Shaded-relief SRTM topographic map of the central Doruneh fault showing the four late Quaternary slip-rate measurement sites (a–d) along with the main towns and villages. The fault trace is marked by a red line.

the two-channel margins on the downstream side. When more than one displaced stream is present within a landform, we make a single best-fit restoration. Further details of our geomorphic interpretations and restorations are provided on a site-by-site basis in Section 5.

For age constraint, we predominantly use infra-red stimulated luminescence (IRSL), with results shown in Table 1, and full data presented in Tables A1 and A2. A full description of the methods is given in the Appendix, which vary slightly from those described in Fattahi et al. (2014). We also performed U-series dating of pedogenic carbonates found at one site. We milled individual growth layers of carbonate from two samples and dated them using the U-Series method. All preparatory and analysis steps are as reported in Gregory et al. (2014), using an isochron-derived initial Thorium composition to correct for detrital component in the samples. Additional details of sampling and analysis are given in the Appendix. The U-series ages are presented in Table A3.

#### 4. Decadal Strain Accumulation From InSAR

We used SAR images from the ASAR instrument (5.6-cm wavelength) on board the ENVISAT satellite to investigate the interseismic deformation across the Doruneh fault. In the “image mode” of the ASAR instrument (swath of 100 km), the studied area is covered by several tracks of the satellite (Figure 1b).

We chose to use 400-km-long interferograms to be able to integrate regions far from the fault trace, in contrast to an earlier study of Pezzo et al. (2012) that considers only 100-km interferograms centered on the fault trace and does not correct for DEM errors and atmospheric effects. The 100-km-long strips of data used by Pezzo et al. (2012) may be too short to discriminate between the long-wavelength orbital error signal and the elastic interseismic deformation around the fault. InSAR analysis by Pezzo et al. (2012) suggests that ~5 mm/yr of displacement accumulates on the fault below 10-km depth in the central part of the Doruneh fault. They also modeled the slip as not purely strike-slip (left-lateral) but also with a significant thrust component.

**Table 1**

*Feldspar IRSL Ages Using a Central Age Model and Corrected for Fading Using a Correction Averaged Between Samples From Each Individual Catchment (See Appendix for Full details)*

Sample no.	Site	Fan	Material	Corrected age	Age $\pm$ (1 sigma)
Kashmar 1	Site C	F2	Silt overlying alluvial gravel	98.6	7.3
Kashmar 2	Site C	F2	Silt overlying alluvial gravel	89.2	6.8
Kashmar 3	Site C	F1	Silt lens in alluvial gravel	26.3	1.8
Kashmar 4	Site C	F1	Silt lens in alluvial gravel	19.6	1.4
Kashmar 5	Site B	F3	Base of slit overlying gravel	130.9	13.0
Kashmar 6	Site B	F3	Alluvial gravel	136.4	14.1
Kashmar 8	Site B	F2	Sandy lens in alluvial gravel	96.9	8.9
Kashmar 9	Site B	F2	Sandy lens in alluvial gravel	96.4	8.5
Kashmar 10	Site A	F2	Silt lens in alluvial gravel	70.7	14.2
Kashmar 11	Site A	F2	Silt lens in alluvial gravel	69.7	12.4
Kashmar 12A	Site A	F2	Silt lens in alluvial gravel	62.5	11.5
Kashmar 12b	Site A	F2	Silt lens in alluvial gravel	63.7	10.8

*Note.* The samples are separated by catchment (Site) and by the fan surface sampled, with the different generations of fan preserved at each site labeled from F1 (youngest) to F3 (oldest). We do not assume that there is direct correlation in age between fans F1, F2, and F3 between sites.

#### 4.1. Processing

Raw radar images from 2003 to 2010 (Processing Level 0) were processed with ROI\_PAC software (Rosen et al., 2004) using the NSBAS package (Doin et al., 2011). The topographic phase contribution was estimated from the SRTM Digital Elevation Model (DEM) at 90-m spatial resolution (Farr et al., 2007). Precise DORIS orbital data for the ENVISAT satellite provided by ESA were used for interferometric processing. We produced single look complex (SLC) images with a common Doppler frequency band. A single master image was chosen following the approach of Zebker and Villasenor (1992) and Hooper et al. (2007), and all other SLCs were co-registered in the master image geometry using the DEM. We processed all possible interferograms having baseline differences less than 500 m to minimize de-correlation of the signal.

The perpendicular baseline distributions of the available images through time are given in Figure A1. A small baseline means that the two images were taken from a close point of view, which optimizes the quality of the InSAR signal. An important factor that affects the coherency of interferograms in our study is the presence of sand dunes. The areas of sand movement change rapidly through time, resulting in very low spatial coherence in interferograms spanning several years, such that the phase cannot be unwrapped across the whole interferogram.

The trade-offs of the tectonic signal with orbital errors and atmospheric phase delays make it necessary to correct orbital, DEM residual errors and stratified tropospheric delay (Massonnet & Feigl, 1998; Zebker et al., 1997). The DEM residual error can be reduced by selecting only interferograms with perpendicular baselines lower than 500 m and temporal baselines lower than 4 years (Ducret et al., 2013). The unmodeled orbital errors in the flattening step can be removed using a best-fitting ramp in range, followed by a best-fitting ramp in azimuth. More complex models could have been used, but we preferred the ramp model to avoid removing the expected interseismic signal located around the fault. The interferograms are then averaged by a factor of 4 in range and of 20 in azimuth, filtered using a power spectrum filter (Goldstein & Werner, 1998), and unwrapped using a branch-cut algorithm (Goldstein et al., 1988).

After these successive corrections, the most important source of errors in this area of Iran is the change in atmospheric conditions between acquisition dates. For example, track D163 (Figure 1b) covers a desert area in the south, mountains in the middle of the image, and moderate topography in the northern part of the track. The tropospheric delay can be split into two components, stratified and turbulent. The turbulent component can be assumed to be distributed randomly both in space and time and can be reduced by stacking or by smoothing during time series analysis. However, the stratified component can cause systematic

errors and should be removed before the time series analysis. In this study, we used the ERA-Interim global analysis to correct for atmospheric effects (Berrada Baby et al., 1988; Doin et al., 2009; Jolivet et al., 2011).

The global atmospheric model provides meteorological parameters (temperature, water vapor, and dry air partial pressure) on a 75-km grid, four times a day. The first step is to select the meteorological parameters at the time step that is closest to the SAR acquisition time, which is at 6 a.m. for descending tracks and 6 p.m. for ascending tracks in our case. The delay map is obtained in two steps: The first step consists of an interpolation of pressure, water vapor partial pressure, and temperature onto height profiles for each ERA-I grid node using a spline interpolation. These interpolated parameters are used to predict the LOS tropospheric delay as a function of elevation on each ERA-I grid node. These LOS delay profiles (function of height) are then horizontally interpolated to the resolution of an SRTM DEM with a bilinear interpolation. For each point (with  $xyz$  position) from the DEM, the LOS delay value at that location is then selected. These values are used to produce a predicted delay map. These delay maps at acquisition date can be combined to obtain a differential delay map for each interferogram. Figure A1 presents an example delay map for two dates and their corresponding differential delay map.

GPS data can independently validate our ERA-Interim delay correction of interferograms. GPS phase measurements are processed using GAMIT/GLOBK to derive tropospheric delay parameters (Zenith Total Delay, ZTD) for the individual stations of the network for each ENVISAT acquisition date. We performed the process in two steps. First, the tropospheric delay was determined together with the site position. Second, the site position was fixed to the average position for that day, and only the ZTD was estimated. We follow this method as simultaneous estimation of height and ZTD is less reliable as ZTD is correlated with height, and variations of ZTD can lead to errors in height estimation.

#### 4.2. Time Series Analysis

To estimate interseismic deformation from interferograms, we used the small baseline InSAR (SBAS) technique (Berardino et al., 2002) to generate a time series of ground deformation. Corrected interferograms are inverted to solve for the phase of successive images using a least-squares inversion method (Cavalié et al., 2007). We added two smoothing constraints on the SBAS time series analysis (Cavalié et al., 2007; Schmidt & Bürgmann, 2003). The first is the temporal smoothing constraint, which is introduced as it is difficult to make any other a priori assumption on the deformation behavior with time for the Doruneh fault. The second constraint is related to the residual DEM error. Note that although these errors might be negligible for baselines of less than 300 m, they may cumulate in the inversion as the cumulative baseline reaches  $\sim 2,000$  m. Then the inversion system becomes:

$$\begin{pmatrix} W.\Delta\Phi \\ 0 \end{pmatrix} = \begin{pmatrix} W.A & W.b \\ \gamma^2 \omega_i \frac{\partial^2}{\partial t^2} & 0 \end{pmatrix} \begin{pmatrix} W.\varphi \\ e_{DEM} \end{pmatrix}$$

where  $b$  is the perpendicular baseline vector,  $W$  is the weight,  $e_{DEM}$  is the proportionality coefficient between phase and baseline due to the DEM error,  $\gamma$  is the smoothing coefficient introduced to penetrate the minimum curvature constraints  $\frac{\partial^2 \varphi}{\partial t^2}$  (where  $t$  is time), and  $\omega_i w_i$  is the weighting factor that can be 1. The aim of the time series can be either the temporal evaluation of ground deformation or Atmospheric Phase Screen (APS) removal. The first option can be homogeneous across the time series by assuming  $\omega_i = 1$  and option two can be homogeneous across the time series by considering  $\omega_i = \bar{\Delta t}_i^2$  (where  $\bar{\Delta t}_i$  is the mean time interval across the five-point differential operator). Cavalié et al. (2007) find that if the weighting factor is the intermediate solution ( $\omega_i = \bar{\Delta t}_i^2$ ) then the APS removal is not negligible for widely spaced acquisitions and the ground motion will not vary too much between densely spaced acquisitions. This inversion is then applied to a very large number of pixels using a least-square inversion (Cavalié et al., 2007) to estimate the long wavelength of the tectonic signal due to the interseismic deformation of the Doruneh fault.

### 4.3. Results

Figure 3 shows the mean velocity map for six tracks that cover the Doruneh fault from west to east along with their corresponding RMS misclosure maps (see Figure 1 for location of tracks). The RMS misclosure map is not directly a measure of uncertainty of the LOS mean velocity map, but rather gives the relative accuracy of the different parts of the interferogram. It is a measure for each pixel of the misclosure of the unwrapped interferometric phase (expressed here in mm) through the network of interferograms. It is very useful to help detect unwrapping errors, which appear to be significant at about 2 mm, in some of the tracks. Profiles through each of the velocity maps are shown in Figure 4.

We performed a close visual examination of the velocity maps to look for sharp variations located exactly along the fault trace, which may be representative of shallow fault creep, but none was found. Local deformations related to subsidence phenomena were found in some valleys. Below we describe the velocity maps for each track, from west to east.

**Track A156:** *Irregular sampling in time through the network (Figure A1) means that the velocity map is strongly dependent on two images (both in 2010), such that we are unable to detect a tectonic signal with reliability. A long wavelength signal that is consistent with left-lateral movement is seen in this track, but the signal is not centered on Doruneh fault.*

**Track D206:** *As with track A156, irregular sampling in time through the network means that the velocity map is strongly dependent on two images (2008 and 2010). At first order, however, the regional phase gradient is similar to that seen in A156 and is consistent with a left-lateral strain accumulation. However, the long wavelength signal is oblique with respect to the fault trace and in addition there are strong local deviations such as the two red patches south of the Fault that shown in 3. According to the RMS misclosure map, these red patches may be due to unwrapping problems, and also may affect the northern part of the interferogram.*

**Track D435:** *The phase gradient across track D435 is located exactly on the Doruneh fault; however, it seems there are unwrapping problems in this track as shown by the RMS misclosure map. Indeed, in most of the interferograms of this track, it was necessary to bridge manually between patches of unwrapped phase in order to make the link between the northern and southern part of the interferogram, which can be the source of errors. The high value of RMS misclosure causes us to be careful in interpreting this phase variation across the fault. Apart from these limitations, this track is also compatible with a left-lateral displacement of the Doruneh Fault.*

**Track D163:** *This track has a similar unwrapping problem as in track D435, with higher RMS misclosure in northern part of the track and lower coherence. No clear interseismic signal can be seen in the mean velocity map, which shows discrepancies with track D435 in their overlapping area.*

**Track D392:** *Track D392 shows a long-wavelength signal consistent with left-lateral displacement, and with a relatively low RMS misclosure. A profile along track D392 (figure 4) shows a change in line-of-sight velocity of 1.5 mm/yr that is consistent with left-lateral strike-slip, but the arctangent shape is centered ~10-km south of, rather than on the, Doruneh fault. We note, however, that there is no corresponding tectonic signal on neighboring tracks to the west (D163) and east (D120). Also, the permanent GPS station THED north of the Doruneh fault (figure 1) shows 1.5 mm/yr of subsidence probably related to ground water extraction, further complicating the tectonic interpretation.*

**Track D120:** *Track D120 has the largest number of images and the best network of interferograms, but shows no discernible signal whilst also having lower RMS misclosure values with respect to the other tracks.*

At the first order, the InSAR measurements are compatible with left-lateral displacement (e.g., in tracks A156, D435, and D392), but in each case, the signal is not centered on the Doruneh fault. In some tracks, our results are affected by unwrapping problems as highlighted, for instance, by the increased RMS misclosure in track D435. We have also found that differences in the signal within overlapping portions of adjacent tracks are significant, and of a similar size to the expected range of interseismic deformation that we aim to measure. The inconsistencies between the signals may be due to imprecise correction of DEM, orbital, and stratified atmospheric errors, or correlation between the interseismic tectonic signal and the topography on any individual track, which will cause our corrections to be biased, by removing part of the tectonic signal

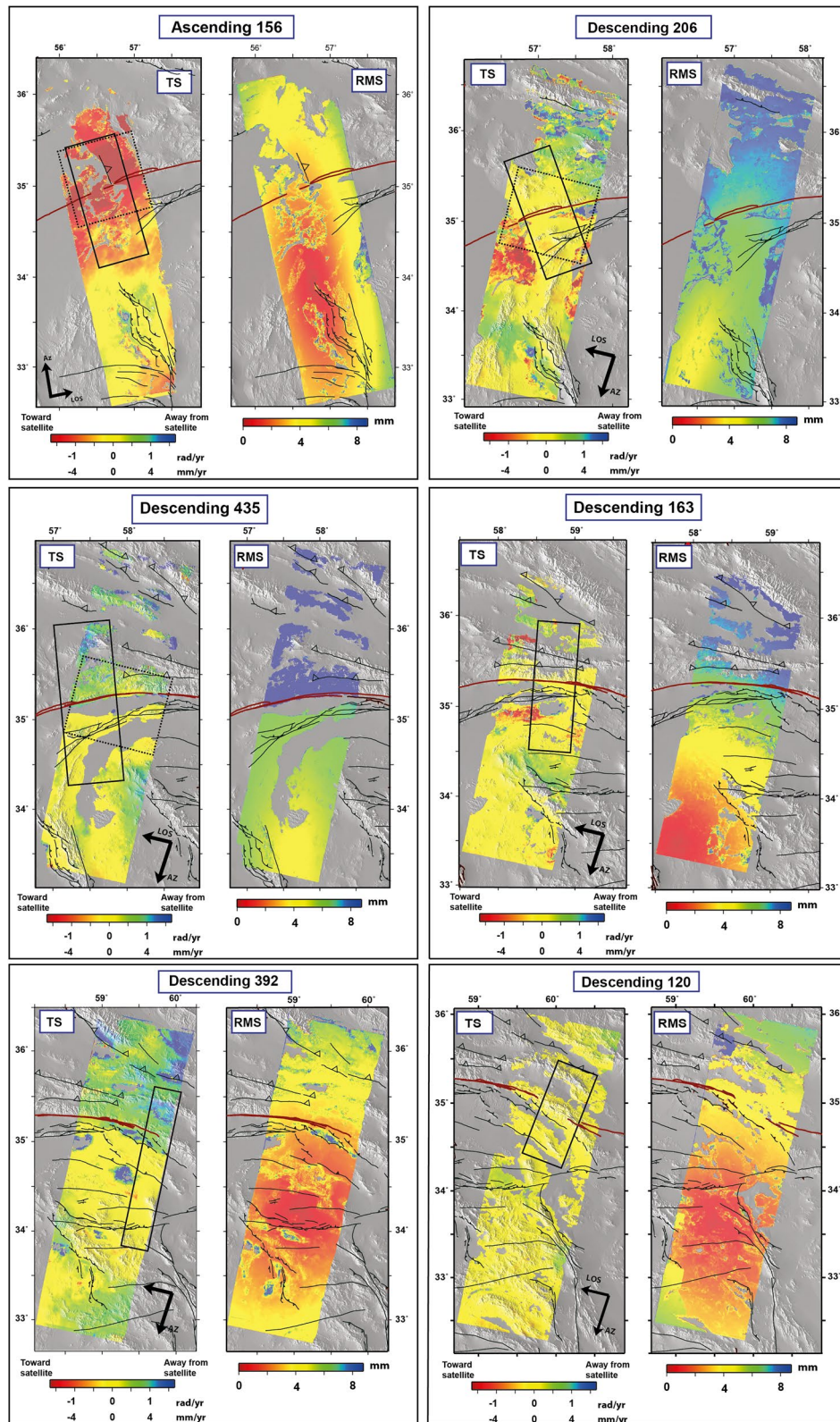


**Figure 3.** Mean line-of-sight (LOS) velocity maps (TS) and root mean square misclosure maps (RMS) for the one ascending (A146) and five descending tracks (D206, D435, D163, D392, and D120), arranged from west to east. The Doruneh fault is shown in red to distinguish it from other active faults. The dashed rectangles show the locations of SAR images used in the study of Pezzo et al. (2012). The solid rectangles represent the locations of profiles shown in Figure 4, with the profiles drawn along the long axis of each rectangle, with data values across the rectangle width projected onto it. SAR, synthetic aperture radar.

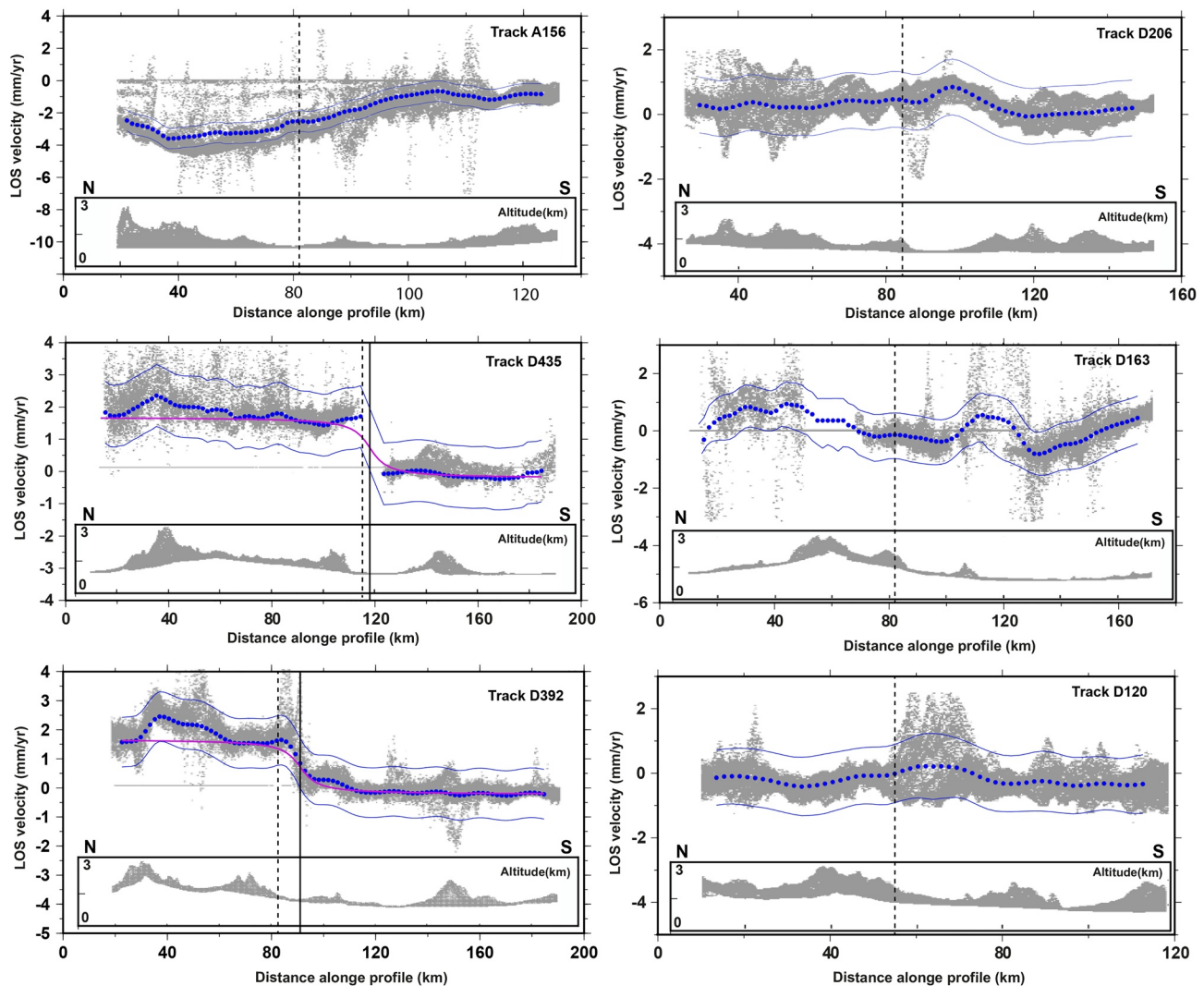


**Figure 4.** (a) Line-of-sight velocity profile (gray dots) with average (thick blue lines) and two-sigma envelope (thin blue lines). The profile boxes are shown in Figure 3. The vertical dashed black line in each profile shows the mapped position of the Doruneh fault. The vertical black line on the profiles from Tracks D435 and D392 is positioned at the center of the SAR signal, which is displaced southward of the mapped fault trace in both cases. The other tracks do not show signals consistent with strain accumulation. An altitude profile is shown beneath each line-of-sight velocity profile. SAR, synthetic aperture radar.

or by adding artificial signal. We conclude that there is no signal of interseismic strain accumulation across the Doruneh fault visible above the level of noise in our data.

As the overlapping portion of two adjacent descending tracks should give very similar ground displacement measurement (the variation due to the slightly different look angle is small), we can compare the overlapping bands to give an estimation of the uncertainty of the InSAR measurement, and hence place a bound on the maximum tectonic signal that might be concealed. The comparison between neighboring tracks D206 & D435 and D163 & D392 is about 1 mm/yr in the LOS direction while this comparison between D435 & D163 and D392 & D120 is in the range of 1–1.5 mm/yr in the LOS direction.

From this comparison, we make a rough estimate of  $\sim 1.5$  mm/yr in LOS uncertainty at the  $\sim 100$ -km scale of the interseismic signal we are looking for. Taking into account a simple model of left-lateral displacement, the largest LOS difference of 1.5 mm/yr between tracks is equivalent to  $< 4$  mm/yr of horizontal velocity. Assuming that the slip on the fault is dominated by left-lateral displacement, we argue that the slip rate of the Doruneh fault cannot exceed 4 mm/yr and is likely to be in the range of 1–3 mm/yr (corresponding to the range 0.5–1 mm/yr in LOS that we estimate as the uncertainty for the majority of tracks).

This very rough estimation does not take into account the possible lateral variation of the slip rate along the fault, and the possible thrust component on the fault, which, assuming southward-verging thrusting, would potentially detract from the strike-slip signal in all descending tracks, and add to the strike-slip signal in ascending tracks. However, given that tracks A156 and D206 overlap, but possess similar velocity maps, we do not consider that any thrust component is important to the overall signal.

## 5. Late-Quaternary Slip-Rate

The four study sites are described from west to east and labeled A–D (see Figure 2). At each site, the different generations of alluvial fans (labeled “F”) and river terraces (labeled “T”) are differentiated by number, with the “1” assigned to the youngest. Field photographs of the sample pits are included as Figure 5. Summary age, displacement, and slip rates from each individual site are summarized in Table 2.

### 5.1. Site A: The Shesh Taraz River

#### 5.1.1. Site Description

The geomorphology of the Shesh Taraz river was first described by Giessner et al. (1984). The present-day river channel is incised into the surface of a well-preserved alluvial fan (F1, Figure 6). Lowering of the river bed occurred in discrete periods, leading to the development of several inset river terraces. Two of the most extensive (T2 and T3) are shown in Figure 6. A higher inset level (T1) is separated from the F1 surface by a low riser at the fault, and merges with F1 downstream. Two older generations of alluvial fans (F2 and F3) are also preserved, with the intermediate one (F2) truncated by the Doruneh fault and forming a scarp ~10-m high (Figures 6 and 7). The eastern boundary of the F2 fan is offset where the edge of the Tigh-e-Ahmad pressure ridge has been displaced by 200 m (Fattahi et al., 2007), to which we add an uncertainty of  $\pm 50$  m.

The terraces of the Shesh Taraz river cover a small left-step and pull-apart basin along the Doruneh fault (Figures 6b and 7). Within the pull-apart, Fattahi et al. (2007) identify left-lateral stream displacements of ~5 m on three streams incised into the T2 terrace surface. The two main strike-slip segments that define the margins of the pull-apart are connected by a series of short NE-SW scarps, across which streams do not appear to be displaced laterally, and presumably involve predominantly normal slip. Within the pull-apart, all the faults, including the main strike-slip strands, possess vertical components of slip. East of the pull-apart, the vertical component of slip is small, though not negligible, and has generated a south-facing scarp of ~10-m high in older (F2) terrace material (Figure 7). The faults can be traced on all surfaces except the present river bed, showing that the last motion postdates abandonment of the lowermost river terrace.

The above observations confirm that the fault motion is predominantly left-lateral, and that the last slip postdates the youngest of the several inset river terraces. Fattahi et al. (2007) investigated the terrace sequence on the eastern bank of the Shesh Taraz river where there is a relatively simple fault trace, and where left-lateral motion is most likely to have been preserved in the geomorphology as the downstream parts of the terraces are moved away from the active river channel (e.g., Cowgill, 2007; Van der Woerd et al., 2002). Fattahi et al. (2007) measured an offset of  $22 \pm 1$  m in the T2-T1 riser from topographic profiles drawn through the terraces on the northern and southern sides of the fault. Our analysis of Quickbird imagery suggests the riser offset is a little larger, at  $25 \pm 5$  m (Figure 8a).

A common problem with the use of terrace riser offsets to infer fault displacement is the ambiguity in whether to associate the offset with the abandonment age of the upper or lower terrace tread. Lateral displacement of geomorphic features on the terrace treads, however, provides an independent check on whether significant erosion of the terrace riser has occurred (e.g., Cowgill et al., 2007). Fattahi et al. (2007) estimate apparent 25 m displacements both of a stream channel on the upper fan surface, and of the apex of an abandoned channel levee on the upper fan surface. The stream channel is visible in Quickbird satellite imagery (Figure 8a).

Farbod et al. (2011) provide an alternative interpretation of the Shesh Taraz site. In their interpretation, the T2-T1 riser is not displaced by an appreciable amount by fault slip, and is instead simply caused by a tight bending in the river channel margin between two strands of the fault. In Figures 8b–8d, we show close-up Quickbird imagery of the T2-T1 terrace riser. In panel “c,” the scene is annotated to show the interpretation

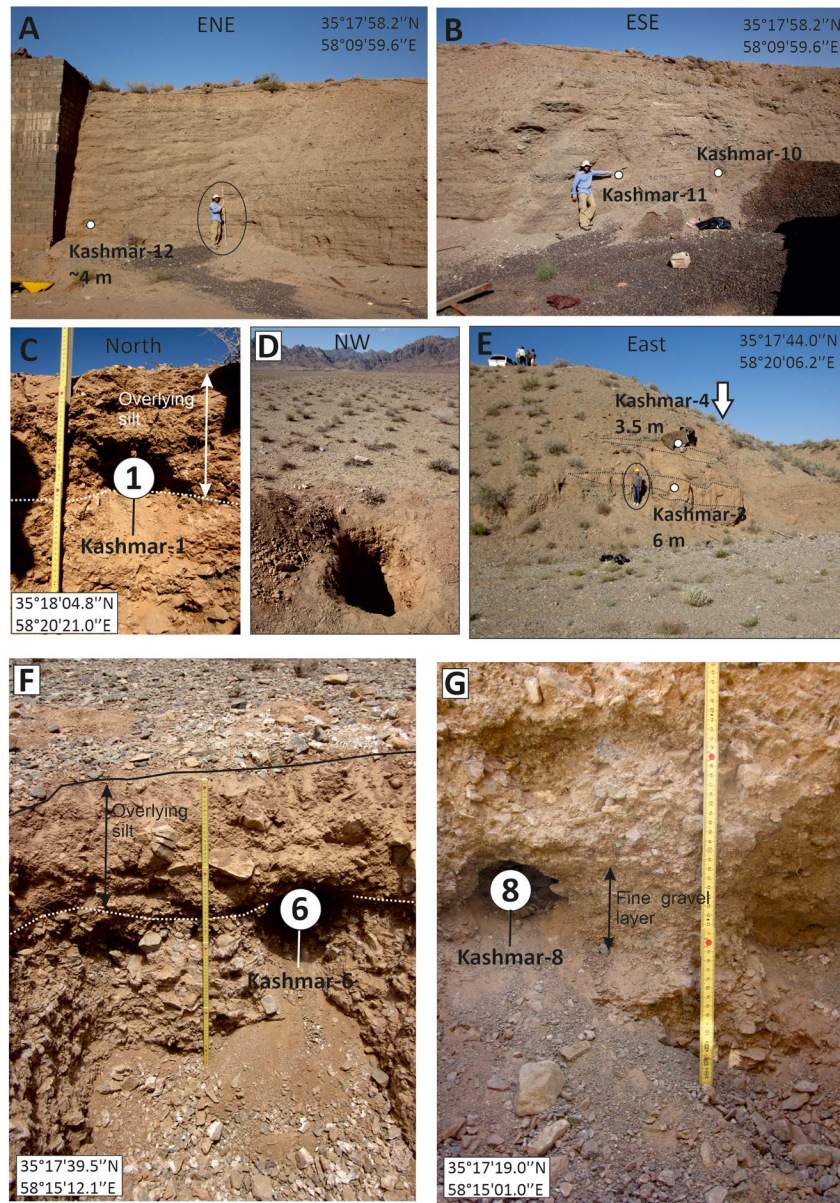


**Figure 5.** Photographs showing sampling locations. See text and later figures for detailed descriptions of each site. (a and b) Sampling from a cutting through the F2 fan deposits at the Shesh-Taraz river (see Figure 7c for location on a map). Sample Kashmar-12 is the deepest, at ~4 m below the surface. (c) Wall of the sample pit in the Khalilabad fan (see Figure 11b for location on a map) from which samples Kashmar-1 and Kashmar-2 were extracted. Both were taken from base of a silt layer that overlies gravels, and hence give a post-date on the end of alluvial deposition. Pedogenic carbonate samples on pebble clasts were taken from a depth of 55 cm within this pit. (d) View of the fan surface with the sample pit in “c” shown. (e) River cutting exposure with two silt layers that were sampled (Kashmar-3 and Kashmar-4). The trace of the Doruneh fault, with uplift to the north and subsidence to the south, is marked by a white arrow. (f) Sample pit in the oldest Nasirabad fan (see Figure 9b for location on a map). Samples Kashmar-5 and Kashmar-6 were taken from this pit from the uppermost part of the gravel sequence. (g) Sample pits from the intermediate Nasirabad fan, from which samples Kashmar-8 and Kashmar-9 were extracted from a finer layer within the gravel sequence.

of Fattahi et al. (2007), whereas in “d” the annotation shows the interpretation of Farbod et al. (2011), who also discount the 25-m left-lateral displacement of a stream and channel levee on the T1 surface, claiming that the apparent displacements result from miscorrelations of features of differing age. The original observations of Fattahi et al. (2007) were based upon field observations, field measurements of displacements

**Table 2**  
Summary of Displacements, Age Data, and Slip-Rate Estimates at the Four Sites

Site	Displacement	IRSL	U-series	Exposure	Slip rate
A	F1	25 ± 5 m	7.4–11.9 (gravel)		1.7–4.1
A	F2	200 ± 50 m	51.0–84.9 (gravel)		1.7–4.9
B	F2	190 ± 50 m	87.9–105.8 (gravel)	34.5 ± 2.2 34.5 ± 4.5 35.5 ± 6.8 52.8 ± 4.9	1.3–2.7
B	F3	Unknown	117.9–150.5 (silt-gravel interface)		
C	F1	60 ± 10 m	18.2–28.1 (gravel)	13.8 ± 2.1 11.5 ± 0.7 22.0 ± 1.6 26.0 ± 2.3	1.8–3.8
C	F2	260 ± 50 m	82.4–96.0 (overlying silt)	91.3–105.9 (gravel)	2.0–3.8 (using full U-series and IRSL range)
D	F2	200 ± 50 m	33.3–62.7 (gravel)		2.4–7.5

Note. Most IRSL ages are from upper parts of the alluvial gravel units (marked “gravel”) and pre-date abandonment of the alluvial fans, though some are from the base of the overlying silt and hence post-date abandonment. Exposure ages are from Farbod et al. (2016).

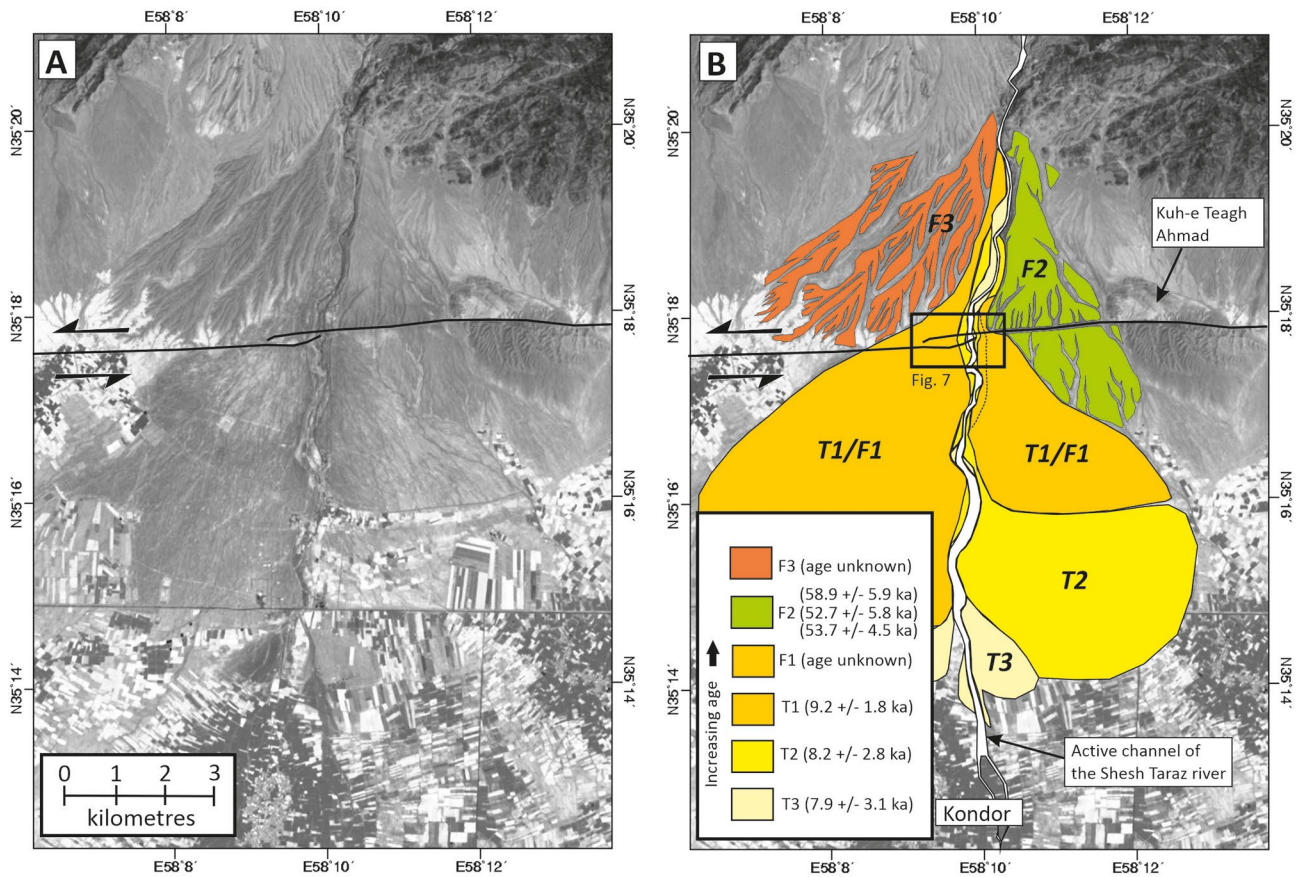


**Figure 6.** (a) ASTER image of the Shesh-Taraz river. The Doruneh fault cuts east-west across the center of the image, forming a small pull-apart immediately west of the main river channel. (b) The same image with interpretation of the geomorphology, along with available age constraints (see text for details). Three main alluvial fan surfaces are recognized on the basis of elevation and level of incision. They are labeled F1–F3, from youngest to oldest. Fluvial terraces incised into the F1 surface are labeled T1–T3. The uppermost fluvial terrace is separated from the surface of fan F1 by a small riser (see Figure 7). T1 and F1 merge downstream to form a single fan, which we label T1/F1. T2 and T3 correspond to alluvial fans formed in the basin interior. The present-day river channel is incised until the village of Kondor, far south of the Doruneh fault. The box represents the area shown in Figure 7.

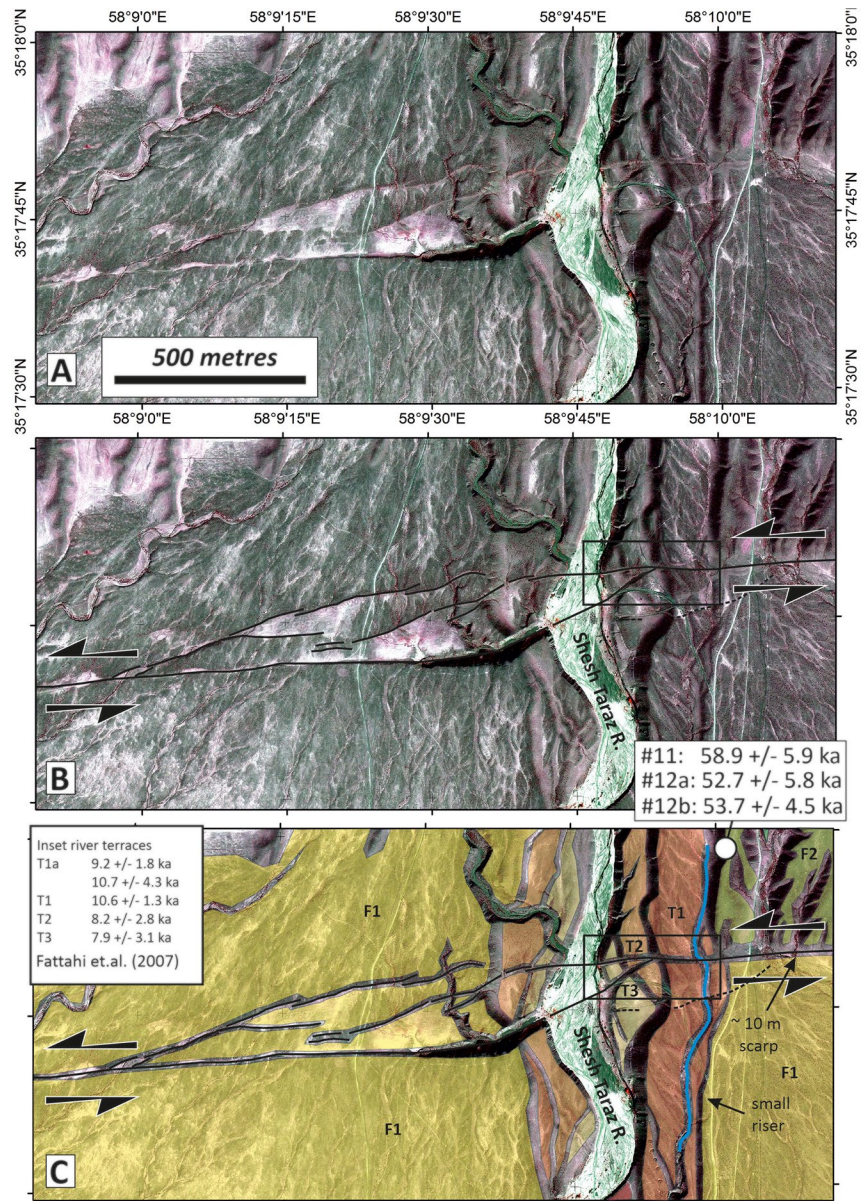


**Figure 7.** (a) Quickbird satellite image of the Doruneh fault trace as it crosses the Shesh Taraz river and alluvial terraces. (b) The same image with the visible fault traces annotated. The faults define a small pull-apart basin. (c) As before, but with the various terrace levels annotated. On the eastern side of the river, the lateral displacements of terrace risers and of a stream on the T1 surface appear to be restricted to a single east-west fault trace that continues to the eastern edge of the image. Age constraints from fan F2 are shown (sampling site shown by white dot, samples Kashmar-11, Kashmar-12a, and Kashmar-12b represented by labels # 11, #12a, and #12b).

using kinematic GPS, and analysis of a DEM made from gridded kinematic GPS measurements. Furthermore, the Quickbird satellite imagery shown in Figure 8 shows both the displaced stream bed on the terrace surface (Figure 8a), and the apparent displacement of the terrace riser (Figure 8c), confirming that the riser and the T1 surface itself is displaced left-laterally by an amount that we estimate at  $25 \pm 5$  m.

### 5.1.2. Age Constraints and Slip-Rate

Fattahi et al. (2007) report IRSL ages for the youngest fan surface and the two main river terraces incised into its surface. Matrix samples were collected from two pits dug into the T1 terrace surface, one on a flat part of the surface, and the other from the apex of a channel levee preserved on the surface. IRSL ages

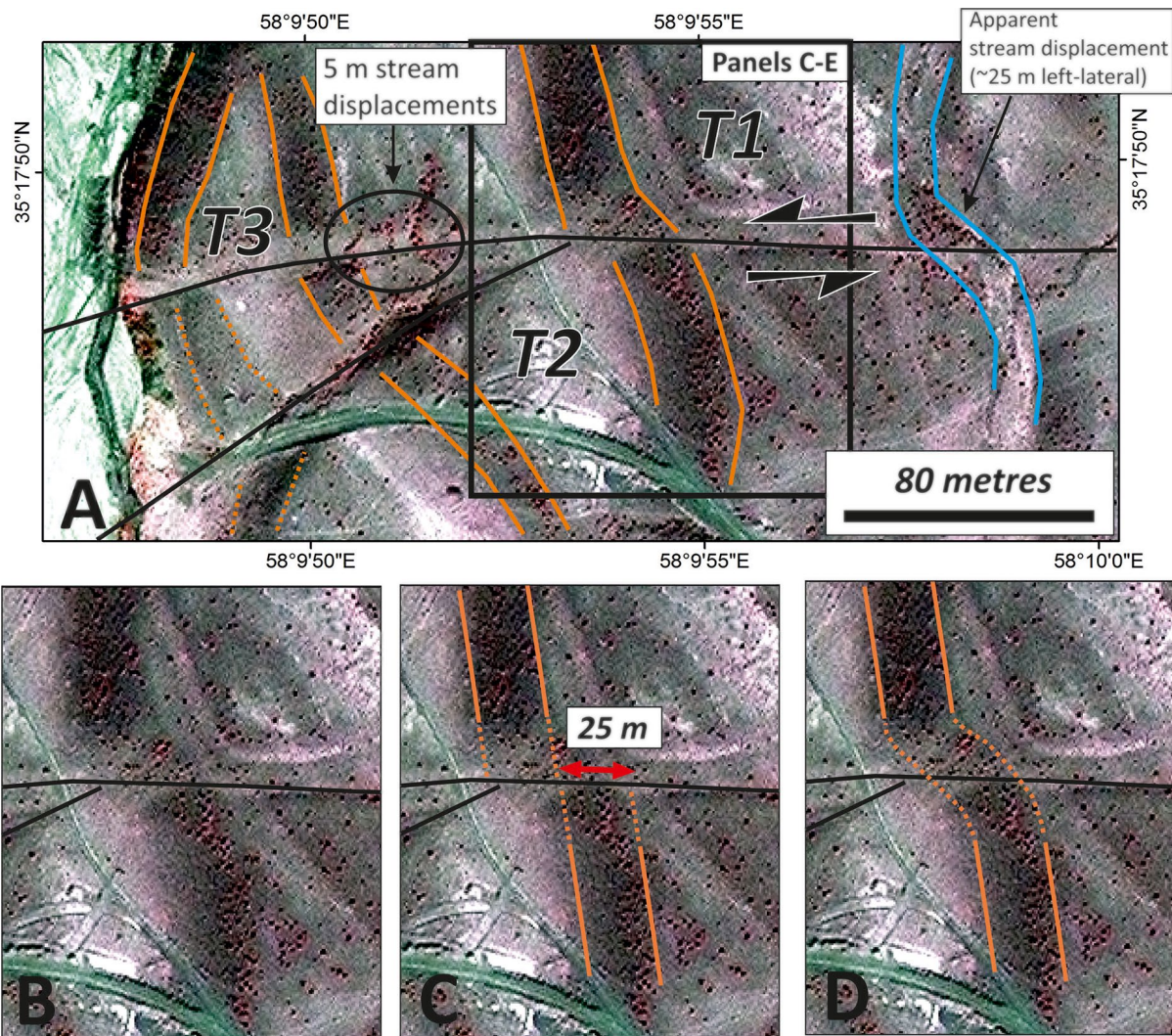


**Figure 8.** (a) Close-up of the Quickbird image shown in Figure 7, showing the Doruneh fault trace cutting through terraces on the eastern side of the Shesh Taraz river. The terrace risers are identifiable due to their dark shading, and we have highlighted their tops and bottoms with orange lines. A small stream apparently displaced by 25 m on the F1 surface is shown, as are two small streams displaced left-laterally by ~5 m (from observations in Fattahi et al. [2007]). (b) A detail of the boxed region in “A,” showing the fault cutting the T1-T2 riser. (c) Interpretation of 25 m of left-lateral displacement of the riser (cf. Fattahi et al., 2007). (d) Interpretation of little to no fault displacement, with apparent displacement caused by fluvial erosion (cf. Farbod et al., 2011).

obtained from feldspar grains from two pits yielded ages of  $10.6 \pm 1.3$  ka and  $9.2 \pm 1.8$  ka, using 90–180  $\mu\text{m}$  grains. IRSL samples from the two lower inset river terraces yielded ages of  $8.2 \pm 2.8$  ka (T2) and  $7.9 \pm 3.1$  ka (T3). Giessner et al. (1984) extracted pottery fragments of unknown age from one of the inset river terraces. A  $25 \pm 5$  m displacement of the upper fan surface combined with the 7.4–11.9 ka age of the fan sediments yields a left-lateral slip rate of 1.7–4.1 mm/yr. At this site, we prefer the use of the “upper terrace” age for calculation of slip rate, as the terrace riser is displaced by a similar amount to a stream bed on the upper terrace surface (e.g., Cowgill, 2007). However, if we instead use the lower terrace (T2) age of 5.4–11.0 ka, the slip rate becomes 1.8–5.6 mm/yr.

We add to the available age data from the Shesh Taraz site by determining the IRSL age of an older generation of alluvial fan (F2) present on the eastern side of the Shesh Taraz river (Figures 5a, 5b, 6b, and 7c). The  $200 \pm 50$  m left-lateral displacement of the F2 fan determined from offset of the Tigh-e-Ahmad pressure ridge combined with its 51–84.9 ka age yield a slip rate of 1.7–4.9 mm/yr.

## 5.2. Site B: The Nasirabad Fan

### 5.2.1. Site Description

The Nasirabad fan is situated at Site B in Figure 2b. Three generations of alluvial fans are observed, along with at least one river terrace inset into the lower of these fan deposits (Figure 9). There are two parallel strands of the Doruneh fault at this site, separated by a distance of  $\sim 100$  m. Farbod et al. (2011) estimate  $400 \pm 10$  m of left-lateral displacement since abandonment of the middle fan surface (which they label “Q2,” see their Figure 12d). Their evidence for this amount comes from the displacement of the riser between the middle and upper fan surfaces (e.g., Figure 9b). They also imply that the main stream channels incised into the middle fan surface (On their figure labeled 1, 2, and 3 on the upstream side of the fault, and 1', 2', and 3' on the downstream side) are also displaced by  $\sim 400$  m. Farbod et al. (2016) estimate a smaller displacement of  $190 \pm 20$  m for the surface, based upon the restoration of streams incised into its surface.

Figure 10 is a close-up Quickbird image centered on the Doruneh fault cutting the three generations of alluvial fan at Nasirabad. The upper panel (Figure 10a) is not annotated for ease of viewing. In Figure 10b, we provide an interpretation of the geomorphology. The three generations of alluvial fans are identifiable from their elevations and degree of dissection and incision by drainage. Our interpretation of the geomorphology of the site differs from that presented by Farbod et al. (2011). Of particular importance are a number of small hills, preserved within the middle fan surface, which from their appearance in the satellite imagery appear to be formed of older Quaternary gravels (highlighted orange in Figure 10b). The row of small hills would restrict the flow of sediment during deposition of the middle fan surface to four narrow passages (which we label 1–4). On the southern, downstream, side of the fault, we observe that the small tributary channels incised into the fan surface define multiple small catchments that converge toward distinct points along the Doruneh fault. In Figure 10b, we have colored these catchments in blue, green, and yellow. The blue and yellow catchments form distinct fan shapes. The green catchment is less distinct, with no discrete convergence point visible. The catchments have been incised by a number of prominent drainage channels that we label “w” to “z.”

In Figure 10c, we have followed Farbod et al. (2016) in restoring 190 m of left-lateral displacement. In this restoration, outlet “1” is adjacent to the apex of the blue catchment on the southern side of the fault, and outlet “4” is adjacent to the apex of the yellow catchment. Outlets “2” and “3” are adjacent to the green catchment. After abandonment of the fan surface, the main stream channels incised into its surface. We note that restoring 190 m of slip approximately aligns the four main channels that have cut into the fan surface on the northern and southern sides of the fault (Figure 10c).

### 5.2.2. Age Constraints and Slip Rate

We excavated pits into both generations of old alluvial fans present on the eastern side of the present-day river (Figure 9b). Both sites were chosen to be on planar surfaces as far as possible from any drainage channels. The older of the two fan surfaces was sampled at 35:17:39.5 N 58:15:12.1 E. This older fan surface is heavily incised, and the pit was dug into a narrow spine between two gullies. The exposed stratigraphy consisted of gravel (composed of both granitic and mafic lithologies) overlain by  $\sim 30$  cm of silt mixed with large clasts. The undersides of clasts throughout the exposed gravel layer possessed long fibrous growths of calcite on their undersides. KASHMAR-6 was taken from the uppermost gravel deposits at a depth of 40 cm and yielded an age of  $136.4 \pm 14.1$  ka. KASHMAR-5 was taken from the base of the overlying silt at 25 cm and yielded an age of  $130.9 \pm 13.0$  ka. A third sample KASHMAR-7 was not analyzed. The two analyzed samples thus bracket the age of abandonment of the fan surface. The amount of left-lateral displacement on this fan displacement is not known, so we cannot estimate a slip rate from these age data.

A 1-m-deep excavation into the younger of the two fan surfaces was made at 35:17:19.0°N 58:15:01.0°E. The exposed stratigraphy was similar in some respects to that seen in the older fan, with a mixture of granitic and mafic gravel clasts overlain by  $\sim 30$  cm of silt. Clast size was variable within the gravels, with some horizons having typical sizes of  $< 1$  cm set in a sandy matrix, whereas other layers had clasts of typical diameter of 5 cm. Occasional large, sub-rounded boulders 10–20 cm are present through the gravel section. Thin carbonate cements were found on the underside of gravel clasts throughout the deposit. At depths of  $> 80$  cm, growths of fibrous calcite were observed on the undersides of clasts.

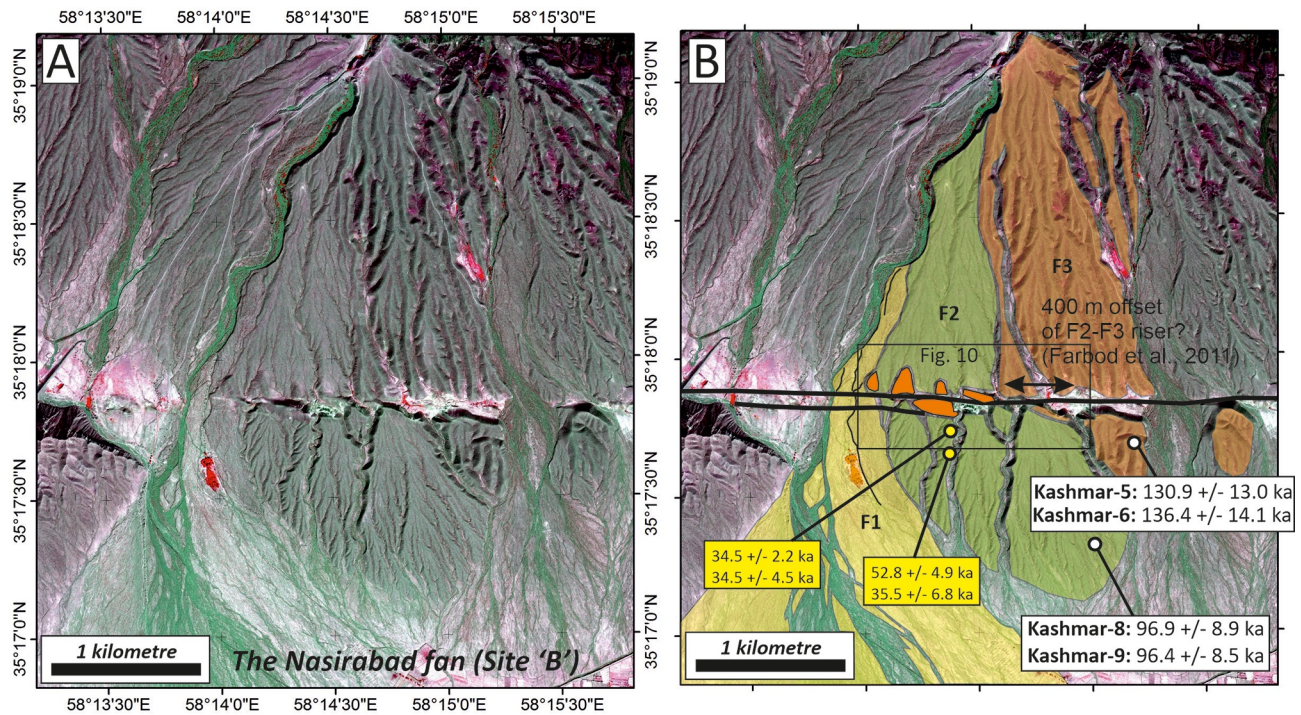


**Figure 9.** (a) Quickbird imagery of an alluvial fan complex near Nasirabad village “Site B.” (b) An interpretation of the geomorphology, along with available age control (white—this paper; yellow—Farbod et al., 2016). Three main fan surfaces are identified, and shaded in yellow, green, and orange from youngest to oldest. Small hills formed of older alluvium are colored in opaque orange.

Two IRSL samples were collected from the center of a 15-cm-thick layer of relatively fine sediment at a depth of 75 cm (Figure 5g). KASHMAR-8 yielded an age of  $96.9 \pm 8.9$  ka and KASHMAR-9 yielded an age of  $96.4 \pm 8.5$  ka (Table 1). These IRSL ages are older than four boulder-top  $^{10}\text{Be}$  exposure ages taken from what we interpret as the same surface by Farbod et al. (2016), three of which gave ages of  $\sim 35$  ka, and a fourth  $52.8 \pm 4.5$  ka. Combined with a left-lateral displacement of  $190 \pm 50$  m, our IRSL ages yield a slip rate of 1.3–2.7 mm/yr.

### 5.3. Site C: The East Khalilabad Fan

#### 5.3.1. Site Interpretation

Two generations of alluvial fans are present on the eastern bank of this catchment (Figure 11). There are two parallel east-west fault traces on the fan surfaces at this site, with the two traces separated by  $\sim 100$  m. The exact motion on the two fault strands at this site may have changed through time, as the region between the two faults has been uplifted since deposition of the older surface, and yet has been down-dropped in the younger surface. The site is labeled as “Site 10” in Farbod et al. (2011). They estimate that the younger of the two fans (which is assigned to be “Q1” in their correlation scheme) is displaced by  $50 \pm 10$  m, subsequently revised to  $60 \pm 10$  m in Farbod et al. (2016). This measurement comes from the apparent offset of a riser between “Q1” and the older surface, which appears to be relatively straight both upstream and downstream of the fault (e.g., Figure 11).

The older of the two fan generations (assigned a “Q2” age in the scheme of Farbod et al. [2011]) is deeply incised, and the upstream and downstream parts of the fan are separated across the fault zone by a steep pressure ridge composed of Quaternary gravels (Figures 11 and 12a). Distributary channels incised into the fan surface appear to be deflected left-laterally across the fault. Farbod et al. (2011) restore these displaced channels with  $260 \pm 30$  m of slip. Farbod et al. (2016) revise this offset to  $200 \pm 50$  m. In Figure 12b, we have labeled the larger incised channels. Those upstream of the fault are labeled 1–3 (following the scheme of

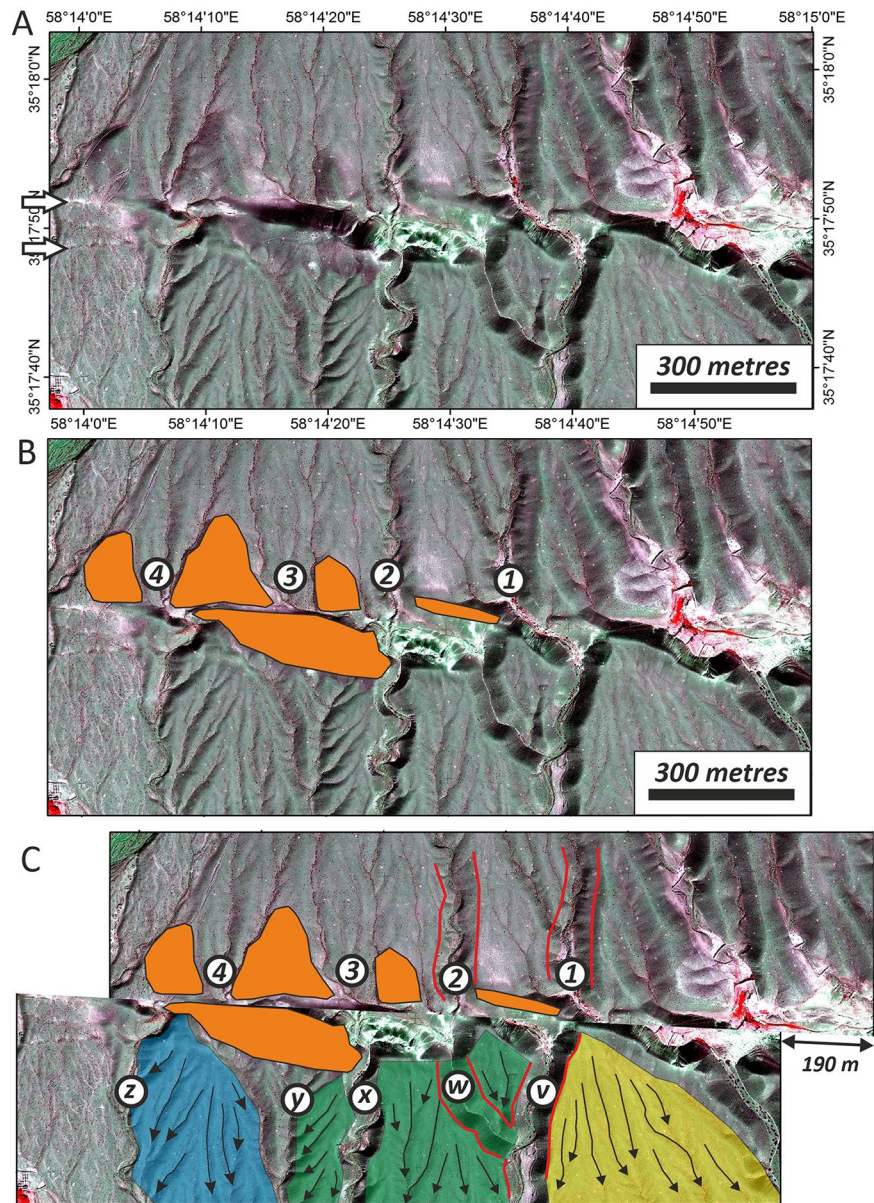


**Figure 10.** (a) Close-up view of the Quickbird imagery within the boxed region in Figure 9b. (b) The same image, with shutter ridges composed of older alluvium marked in orange, and four prominent incised streams that reach the fault in gaps between successive ridges labeled 1–4. The fan surface to the south of the fault appears different to that in the north, with slightly incised drainage networks that appear to converge at the fault. (c) Restoration of  $190 \pm 50$  m of slip appears to align the channels 1–4 on the northern side of the fault with convergence points in the drainage networks south of the fault.

Farbod et al. [2011]). We have also labeled an additional stream (x) that was omitted from the reconstruction of Farbod et al. (2011). On the downstream side, we mark the three main drainage channels as 1', 2', and 3'. We also show a beheaded and abandoned channel that is part of the 2' drainage system (shown as a dotted line).

Apparent left-lateral displacements are interpreted from the stream courses (e.g., Farbod et al., 2011). In Figure 12d, we show the main drainage channels (as described above). Some elements of the drainage network are restored by 130 m of left-lateral slip (shown in orange in Figure 12e). Channels 1 and 1' are aligned. Channel “x” is aligned with the now abandoned second channel of “2.” The easternmost of the

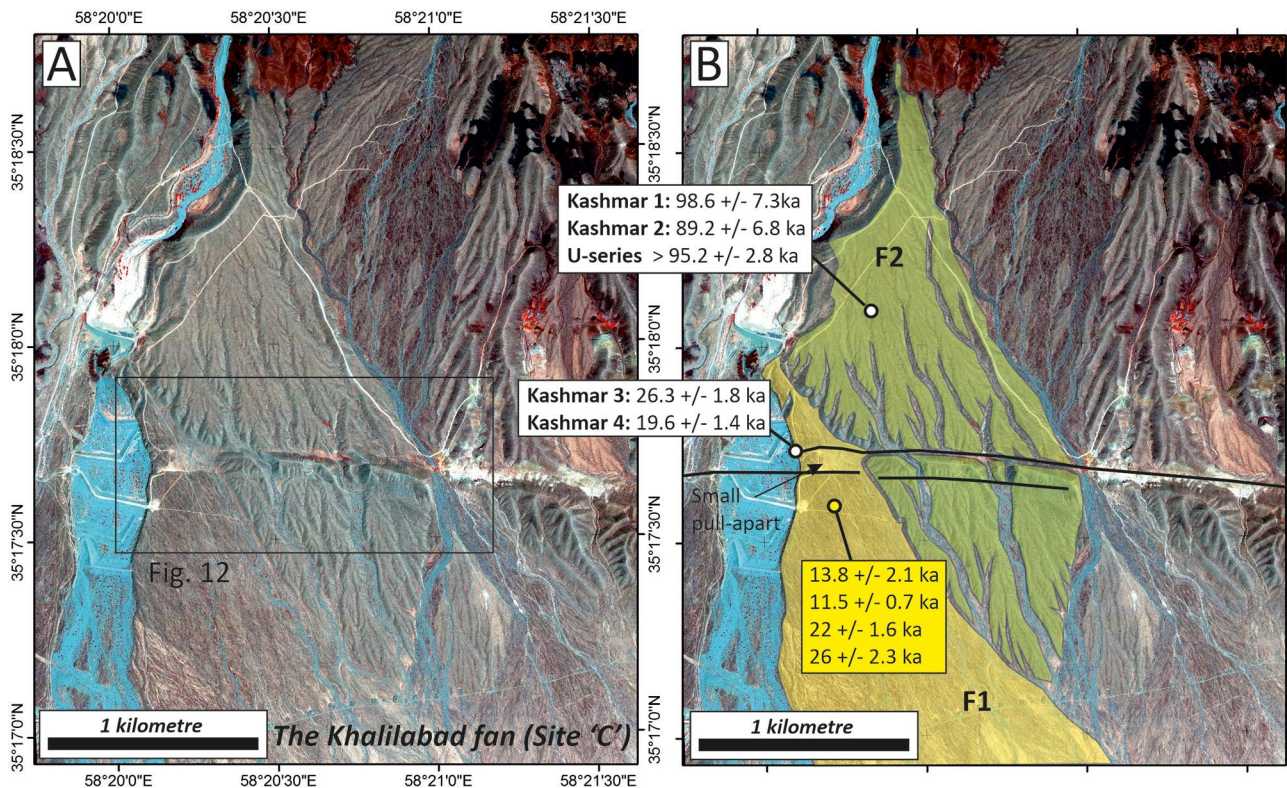


**Figure 11.** (a) Quickbird imagery of “Site C,” close to the village of Khalilabad. (b) Geomorphic interpretation showing the active fault traces and the two generations of alluvial fan present at this site. Age constraints from this study are shown in white, and those from Farbod et al. (2016) in yellow (only approximate location shown).

channels of “2” is aligned with “2.” However, the restoration of 130 m does not restore all drainage features successfully, as shown by those drainage systems in red. Evidence for larger amounts of slip is provided by the western channels of “2,” which have no outlet, and by the remaining left-lateral kink in the course of channel 3–3’.

In Figures 12c and 12f, we have restored the 260 m of left-lateral slip estimated by Farbod et al. (2011), though with a slightly larger uncertainty of  $\pm 50$  m. This larger restoration also works for some elements of the drainage network, in particular realigning 2–2’ and 3–3’. However, channels 1 and 1’ are over-restored, and channel “x” has no outlet. Although coming to the same overall conclusion, our restoration changes in some details from that presented by Farbod et al. (2011), who states that all three of the main drainage channels (1-1’, 2-2’, and 3-3’) are restored by  $260 \pm 30$  m of left-lateral slip (see their Figure 12f). We instead show that 1–1’ is restored by only  $\sim 130$  m of slip, and that the drainage systems associated with channels 2 and X underwent a reorganization after 130 m of slip had accrued. Our restoration favors the original 260 m offset as described by Farbod et al. (2011), rather than the  $200 \pm 50$  m displacement of the fan presented by Farbod et al. (2016), though we note that the two estimates overlap.

Those channels that are successfully restored by  $260 \pm 50$  m of left-lateral slip are those that were not successfully restored by 130 m slip. Our conclusion is that  $260 \pm 50$  m of left-lateral slip has occurred since the earliest visible period of drainage incision, but that the second generation of drainage was incised into the fan surface after  $\sim 130$  m of slip had occurred. It seems likely that the initial drainage network was established soon after abandonment of the fan surface, given that any drainage elements forming a significant time after abandonment would have to cross a topographic barrier between the two parallel fault strands. It is plausible that channel 1’, which shows no more than 130 m of deflection from channel 1, might also date from the establishment of the original drainage network, as the part of the fan surface that would have

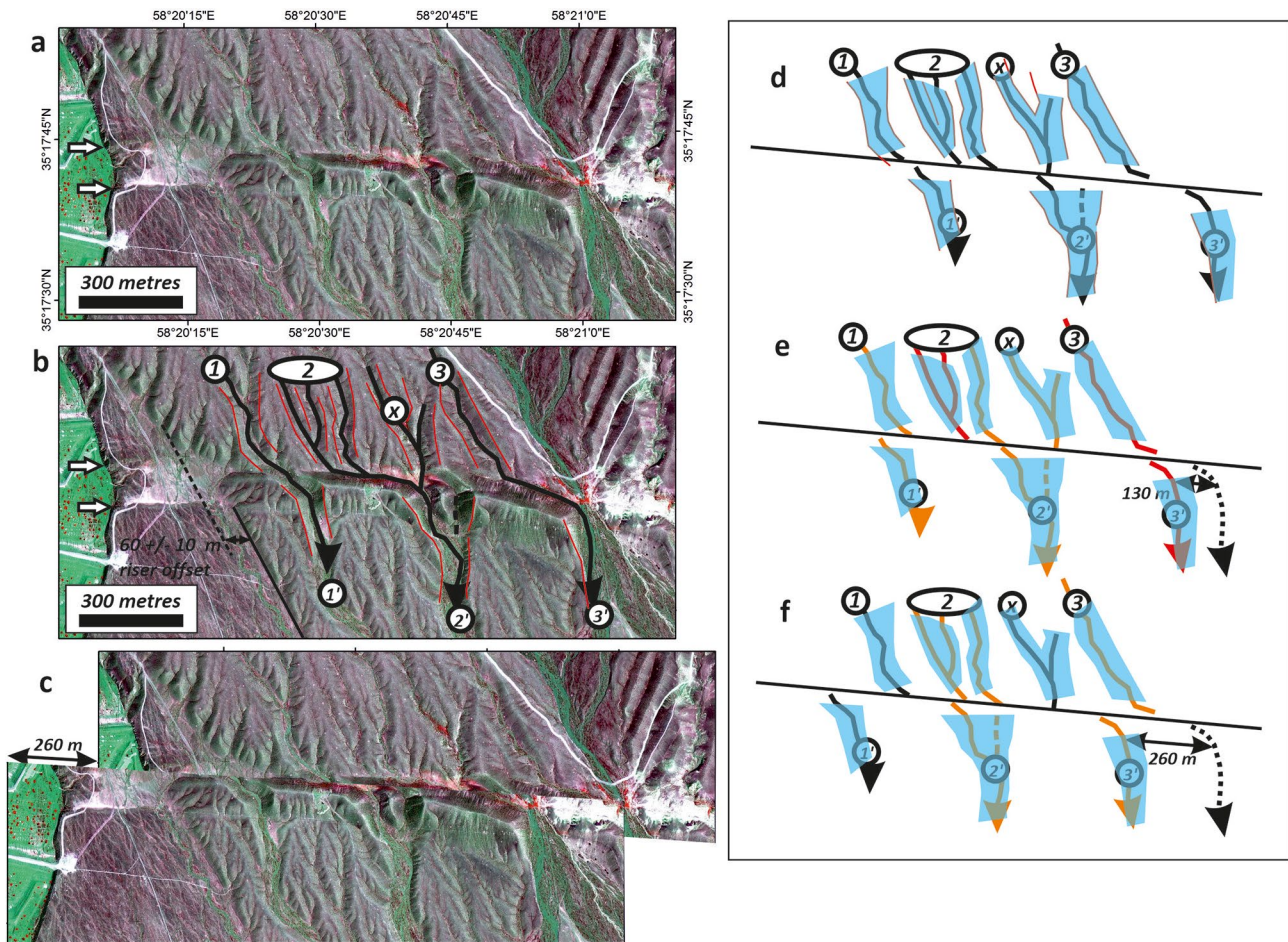


**Figure 12.** (a) Quickbird imagery of the fault crossing older and younger alluvial fan surface at site C (boxed region in Figure 11a). Two closely spaced fault strands are present, marked by white arrows. (b) The same image, but with annotation to show the main drainage systems on the older fan surface (with the bases of the channels in black and the tops in red). A  $60 \pm 10$  m left-lateral displacement of the terrace riser is also shown. (c) Restoration of  $260 \pm 50$  m restores the displaced drainage systems in the older fan surface. (d–f) Restorations using the traced drainage channels shown in “b.” Some channels (in orange) are restored to their original courses with only  $\sim 130$  m of displacement, but others (in red) require  $260 \pm 50$  m.

originally been adjacent to channel 1', on the northern side of the fault, has been eradicated during the emplacement of the younger surface (Figure 12f).

### 5.3.2. Age Constraints and Slip-Rate

We provide ages for both the older and younger generation of alluvial fans at East Khalilabad (Figure 11b). A pit was excavated into the surface of the older fan at  $35:18:04.8^{\circ}\text{N } 58:20:21.0^{\circ}\text{E}$  (Figures 5c and 5d). Natural exposures in the present-day river bank at  $35:17:44.0^{\circ}\text{N } 58:20:06.2^{\circ}\text{E}$  were selected for sampling the younger alluvial surface (Figure 5e).

The river bank exposures through the younger of the two abandoned alluvial fans are shown in Figure 5e. The northern of the two parallel fault scarps, downthrown to the north, is visible in the center of the image. The exposed deposits are mostly coarse alluvium, but two homogeneous silt bodies outcrop on the northern side of the fault. The lower of these two silt bodies is  $\sim 1$ -m thick, and the upper one  $\sim 30$ -cm thick. The fault itself is obscured, but we note that the silt bodies do not extrapolate to the southern side of the fault, and are presumably displaced to beneath the level of the present-day river bed. IRSL samples from the two silt bodies exposed in the river-bank exposure yield ages of  $26.3 \pm 1.8$  ka (sample KASHMAR-3,  $\sim 6$ -m depth in the stratigraphy) and  $19.6 \pm 1.4$  ka (sample KASHMAR-4,  $\sim 4$ -m depth). The two sample ages are in stratigraphic order and, if the sediment deposition rate was constant, imply an age of as little as 10 ka for the surface abandonment itself. Also, we can constrain the maximum age of the surface to be  $19.6 \pm 1.4$  ka,

which assumes very rapid deposition of the upper parts of the stratigraphy. Our IRSL ages are consistent with four boulder-top exposure ages collected from the fan surface by Farbod et al. (2016) and dated between  $11.5 \pm 0.7$  and  $26 \pm 2.3$  ka (See Figure 11b for the four individual sample ages).

The older fan (highlighted in green and labeled F2 in Figure 11b) was sampled with the aid of a 1-m deep pit excavated into the fan surface at  $35:18:04.8^{\circ}\text{N}$   $58:20:21.0^{\circ}\text{E}$  (Figures 5c and 5d). The site was selected to be on a planar section of the fan surface far from any drainage channels (Figure 11b). The fan surface is armored with angular gravel clasts exhibiting a well-formed dark varnish, and there is little evidence of bioturbation and little vegetation cover (e.g., Figure 5d). The upper layer of desert armor is underlain by a 45-cm soil layer, with occasional pebbles set in a predominantly silty matrix. The amount of pebbles set within the silt varies with depth, with very few in the upper 25 cm, and with a larger proportion in the lowest 10 cm of the layer. Below the silt, there is an abrupt transition to coarse gravel with clasts 5–10 cm in diameter. The clasts are mainly of mafic igneous composition. A well-formed carbonate cement consisting of thick rinds on the underside of clasts is present at 55 cm. The carbonate formation is also present in the lowest 10 cm of the overlying silt units (i.e., to a depth of 35 cm from the surface). Two IRSL samples were taken from the silt unit at depths of 30–35 cm. These two samples yield ages of  $98.6 \pm 7.3$  ka (KASHMAR-1, 35-cm depth) and  $89.2 \pm 6.8$  ka (KASHMAR-2, 30-cm depth). We also dated the rinds of carbonate found on the underside of gravel clasts at a depth of 55 cm. Detritally corrected ages are plotted in Figure 13. The data shows a clear correlation of growth at the 92.4–98.0 ka isochron age. A further correlation between samples exists at  $\sim 20$ –30 ka implying a younger generation of carbonate. There is also a single data point at  $\sim 80$  ka, which could either represent an episode of growth, or cross-contamination of the two sample groups. The data strongly suggests the onset of carbonate growth around 100 ka, in agreement with the IRSL ages.

We calculate a slip rate of 2.0–3.8 mm/yr using a left-lateral displacement of  $260 \pm 50$  m combined with the full range of IRSL ages of 82.4–105.9 ka, which are both likely to postdate the alluvial gravel deposition, and are similar to the U-series isochron age, suggesting that both postdate gravel deposition by only minimal amounts of time. Support for an interpretation that formation of the carbonate rinds started soon after deposition of the gravels comes from the lack of carbonate growth from Marine Isotope Stage 5e, at  $\sim 125$  ka. The surface of the younger fan (highlighted yellow and labeled F1 in Figure 11b) is dated between 18.2 and 28.1 ka, yielding a slip rate of 1.8–3.8 mm/yr using the  $60 \pm 10$  m riser displacement of Farbod et al. (2016).

## 5.4. Site D: The Uch Palang Fan

### 5.4.1. Site Description

Drainage incised into alluvial fans at the village of Uch Palang (Figure 13) was described by Wellman (1966) and Giessner et al. (1984), who both use the site to demonstrate the left-lateral nature of the Doruneh fault due to the evidence of cumulative left-lateral slip. The overall morphology of the fan deposit, along with apparent displacements of drainage incised into its surface, has led a number of authors to estimate the left-lateral displacement of the fan surface to be  $800 \pm 50$  m (Farbod et al., 2011; Fattahi et al., 2007; Wellman, 1966). In addition to the apparent drainage displacements, Farbod et al. (2011) state that a line drawn down the apex of the fan is displaced by  $880 \pm 50$  m across the fault, providing independent support for that order of displacement. However, there is little curvature of the fan surface, as visible in their Figure 13, such that any choice of the “apex line” is highly subjective, and hence not useful in constraining displacement of the fan surface.

Walker and Fattahi (2011) note that the majority of stream channels cut into the fan surface can be restored to linear courses with only  $\sim 150$  m of displacement, and suggest that the postulated 800–900 m restoration is an overestimate. Walker and Fattahi (2011) further suggest that the overall shape of the fan, with margins that appear to be displaced left-laterally by 800–900 m, is deceptive. They argue instead that the shape results partly from erosion of the margins of the remnant fan during later periods of river incision and fan deposition.

In Figures 13c and 13d, we show the restoration of Walker and Fattahi (2011), though with a slightly increased offset estimate of  $200 \pm 50$  m.

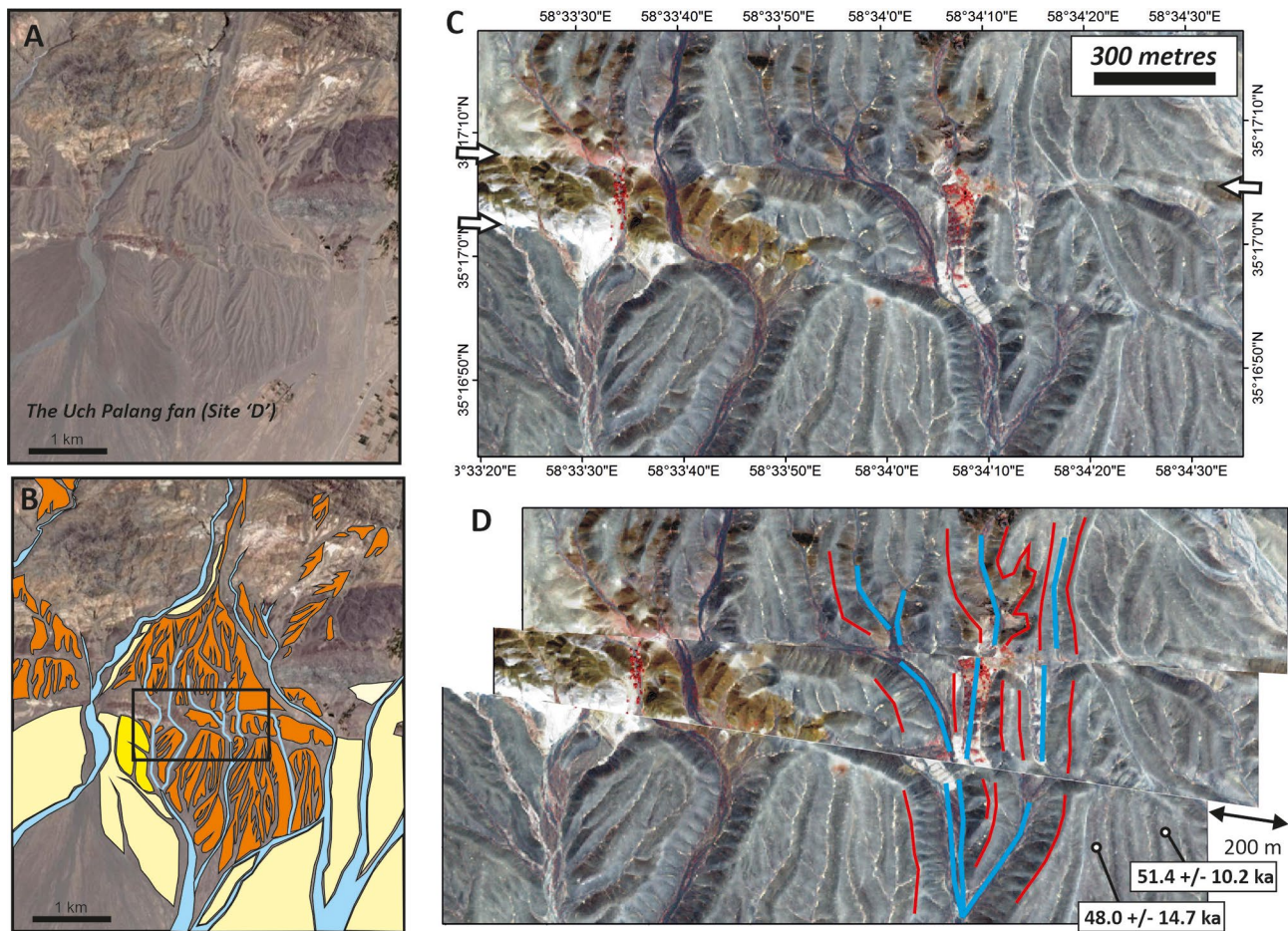


**Figure 13.** (a) The Uch Palang alluvial fan (Site D). (b) Geomorphic interpretation of the site. The oldest fan surface is in orange and the youngest surface in pale yellow. The small surface shown in bright yellow may be intermediate in age. (c) Close up IKONOS image showing the fault crossing the older fan surface. (d) Restoration of  $200 \pm 50$  m restores the drainage channels (channel bases in blue and tops in red) to their original linear shape. Ages from Fattahi et al. (2007) are shown.

#### 5.4.2. Age Constraints and Slip-Rate

Fattahi et al. (2007) provided IRSL ages of  $48.0 \pm 14.7$  and  $51.4 \pm 10.2$  ka from two pits dug into the gravels.  $200 \pm 50$  m of displacement yields a slip rate of 2.4–7.5 mm/yr. The alternative 800–900 m of displacement yields a much larger slip rate of at least 16 mm/yr.

## 6. Discussion

In Section 5, we dated a number of landform features that range in age from  $\sim 10$  to 100 ka, and that are displaced by measurable amounts across the Doruneh fault. The individual slip rate estimates are shown in Table 2. In Figure 14, we show a plot of age against displacement, with data plotted for each of the sites where we have firm constraint on age and displacement. A best-fitting regression line and associated two-sigma satisfy a slip rate of  $2.5 \pm 0.2$  mm/yr when the inversion is fixed to go through the origin. We also performed an inversion that was not constrained to go through the origin, which yielded a rate of  $2.5 \pm 0.3$  mm/yr. It is this value that we use below.

Overall, as all of our sites satisfy a single rate of slip, it indicates that the slip rate has remained constant when averaged over various time periods over the last 10–100 ka. The much faster slip rates proposed by Farbod et al. (2011, 2016) appear to result mainly from miscorrelation of fan surface ages between catchments, combined with overestimation of displacement in at least one case (the Uch Palang site, Section 5.4).

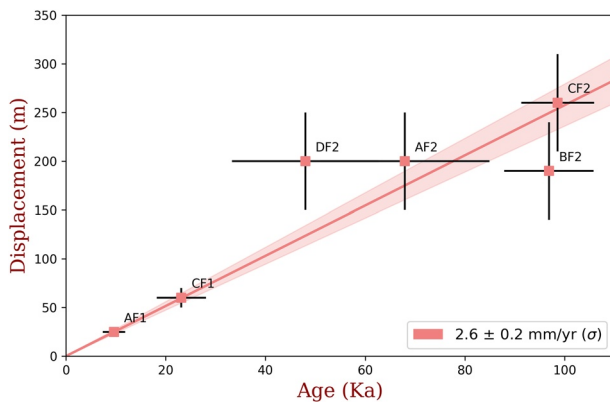


**Figure 14.** Plot of age against displacement for the dated landforms, with each labeled by site and then fan generation (i.e., DF2 = Site D, fan F2). An orthogonal distance regression is fitted to the six data points for which we have reliable age and displacement measurements (these six measurements are shown as red squares, with their uncertainties shown as black bars). The regression takes into account the uncertainties in both age and distance uncertainties (one-sigma for both). The best fit line is shown in red, with two-sigma uncertainty in the regression represented by the pink area. In the plot shown, the best fit line is constrained to pass through the origin. If the best fit line is not constrained to pass through the origin the mean slip-rate does not change, but the uncertainty increases from  $\pm 0.2$  to  $\pm 0.3$  mm/yr.

Constancy in long-term averaged slip rates does not exclude variability over shorter, millennial, time scales. We have therefore compared the long-term rates with measurements of the present-day strain accumulation across the fault, to see whether shorter timescale variations can be inferred from any mismatch between the two. Using InSAR, we find that the present-day strain accumulation on the Doruneh fault is similar, or possibly lower, than its long-term slip rate, with a likely range of 1–3 mm/yr and an upper limit of 4 mm/yr that is lower than suggested in the study of Pezzo et al. (2012). Constraints on the present-day deformation from GPS are varied, but again indicate relatively low (2.5 mm/yr or less) slip rates. Initial results from the Iranian GPS network indicated a left-lateral slip rate of 2–2.5 mm/yr at longitude 58°E decreasing eastwards to 1–2 mm/yr at longitude 60.5°E (Tavakoli, 2007). According to more recent data from the permanent and campaign GPS networks the slip rate is estimated at  $2.1 \pm 0.4$  mm/yr from a rigid block modeling approach, and to  $0.5 \pm 1.1$  mm/yr from the difference of average GPS velocities of stations located on opposite sides of the fault (Mousavi et al. 2013; Walpersdorf et al. 2014). However, the usefulness of both of these approaches is likely to be affected by the sparse and uneven distribution of GPS stations around the fault, and by the presence of multiple active faults within the “blocks” adjacent to the Doruneh fault.

Overall, we see no indications that the slip rate on the Doruneh fault has varied substantially over the last 100 ka. Although present-day rates lower than the long-term average are possible given the existing constraints from InSAR and GPS, the likely maximum present-day rate of strain accumulation

(at  $< 4$  mm/yr) is consistent with the fault slip rates ( $2.5 \pm 0.3$  mm/yr) estimated over time periods of 10–100 ka. It is not surprising that strain accumulation on the Doruneh fault is difficult to determine using the available GPS and InSAR measurements, given the relatively slow rate, the sparse GPS station distribution, and the dominant north-south right-lateral shear that occurs across this part of Iran. Copley (2008), for instance, showed that the slip rate on faults in such regions is difficult to constrain without dense GPS coverage.

In Figure 15, we show east-west profiles of northward-directed GPS velocity relative to Eurasia across north-east Iran (see Figure 1b for profile locations). The profiles show an increase in northward velocity over a distance of  $\sim 400$  km, from zero near the Afghan border in the east, to  $\sim 8$  mm/yr near the western end of the Doruneh fault (near stations ROBA in Figure 15a and BIAJ in Figure 15b). Left-lateral slip on the Doruneh fault, and on other east-west faults of northeast Iran, can accommodate the regional right-lateral shear if they rotate anticlockwise about vertical axes. In Figure 15c, we show a simple model of the faulting in northeast Iran. Using a value of 8 mm/yr for the north-south right-lateral shear, an east-west width of 400 km, and a fault spacing of 50 km returns a slip rate on the faults of 2 mm/yr. A model of left-lateral faulting combined with clockwise vertical axis rotation is consistent with paleomagnetic declination changes measured across northeast Iran (Mattei et al., 2017).

Our study has implications regarding the timing of major range-front alluvial fans in northeast Iran, and for the ability to correlate such landforms between catchments and regionally. Our IRSL and U-series ages suggest periods of fan deposition at  $\sim 125$  ka and in the early Holocene at  $\sim 8$ –10 ka. There are also apparent periods of fan development at  $\sim 80$ –100 ka,  $\sim 50$ –70 ka, which are in broad agreement with the few other existing studies of late Quaternary alluvial fan development across Iran, though the low precision in ages and the small number of dated surfaces prevent us from assigning any confidence to the correlation (e.g., Walker & Fattahi, 2011).

At sites B and C, where we have sampled the same alluvial fans as those dated by Farbod et al. (2016), our IRSL ages are either older, or within the spread of boulder-top cosmogenic  $^{10}\text{Be}$  exposure ages obtained in that study. For the older examples of alluvium dated with IRSL, the closest agreement is with the older end of the spread of  $^{10}\text{Be}$  ages. If the oldest of the boulder ages is closest to the deposition age, it suggests that

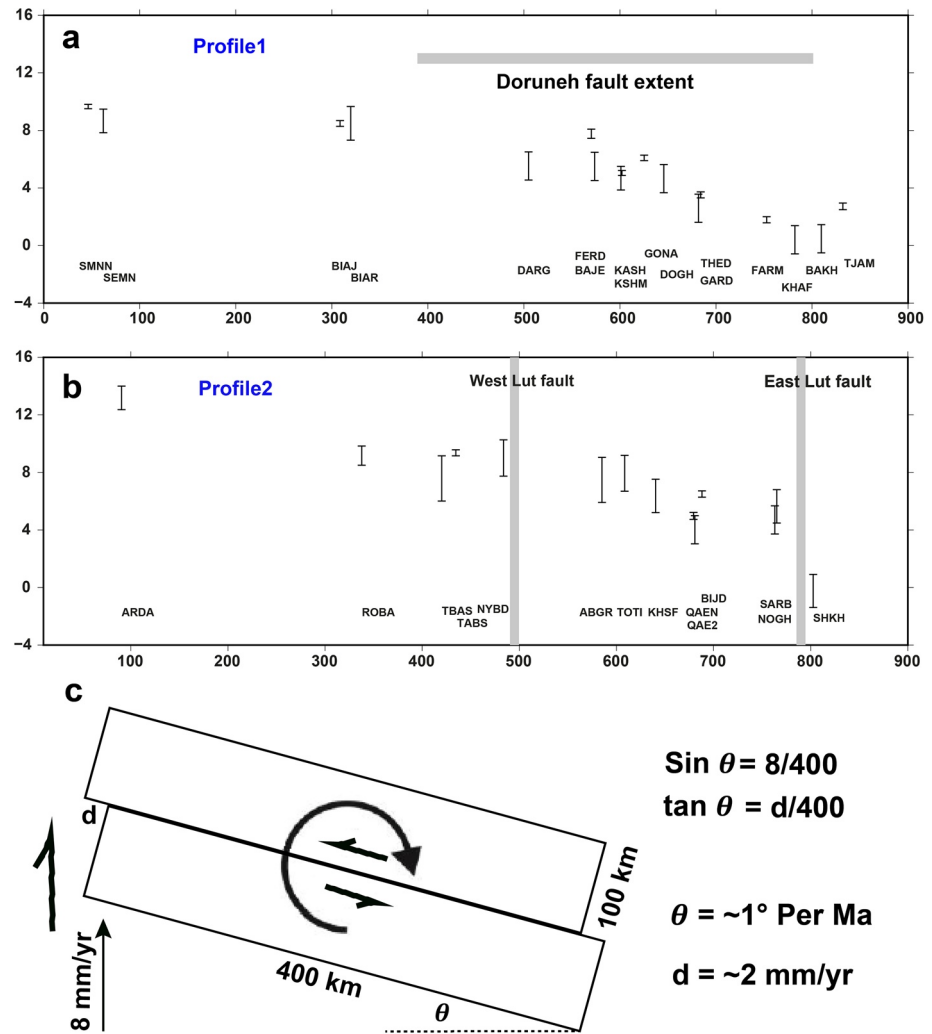


**Figure 15.** (a) East-west profile showing northward-directed components of velocity north of the Doruneh Fault. (b) A similar profile south of the Doruneh Fault, with the positions of the right lateral West Lut and East Lut strike-slip fault zones marked. The two profile lines are shown in Figure 1a. Approximately 8 mm/yr of north-south right-lateral shearing occurs across a region ~400 km in east-west extent. (c) Cartoon adapted from Fattahi et al. (2007) showing how the measured slip-rate on the Doruneh fault can be explained by regional right-lateral shearing and clockwise vertical axis rotation (i.e., bookshelf faulting). We assume there is negligible shortening, as indicated by the two profiles through the GPS in “a” and “b.” The left-lateral slip-rate (d) and clockwise rotation ( $\theta$ ) vary depending on the input block dimensions and rate of N-S right-lateral shear.

post-depositional processes are the dominant control on scatter within the boulder populations, at least in those few sites with independent age control. A similar post-depositional signal can be seen in the full dataset of  $^{10}\text{Be}$  boulder ages in Farbod et al. (2016), which show a general increase in scatter in progressively older surfaces, as seen in their Figure 10, but again show broad agreement with our own chronology of alluvial fan deposition. Although the two sets of age data are consistent, Farbod et al. (2011, 2016), were incorrect in their correlation between fan surfaces between catchments, such that erroneous ages were assigned to fan surfaces in places without direct age control. We therefore highlight the dangers in correlating geomorphic surface between different catchments, and in assuming the ages of individual surfaces without direct age control.

## 7. Conclusion

The Doruneh fault is one the longest faults inside the political borders of Iran, with clear expression in the geomorphology, yet there is large variability in its reported slip rate. We have shown that this variability is likely to arise from inaccuracies in correlation between alluvial fan surfaces along with uncertainties in restoration of displacement of the fan surfaces. Instead, the slip rate appears to have been constant at  $2.5 \pm 0.3$  mm/yr over the last 100 ka. Our result has implications for the hazard posed by the Doruneh fault, for which there is no historical record of earthquakes over much of its length. Our age data and those from  $^{10}\text{Be}$  exposure dating published elsewhere are consistent with widespread alluvial fan deposition at distinct times, though we highlight the dangers associated with correlations between different catchments, where different sequences of fan deposit might be encountered due to incomplete preservation, or due to local differences in the hydrology of individual catchments.

## Appendix A

### A1. Infra-Red-Stimulated Luminescence

All samples were collected by hammering steel tubes into the sediment, either into existing exposures, or from the walls of pits dug by hand. The ends of the tubes were packed tightly with paper and aluminum foil and then sealed with several layers of duct tape. The sealed tubes were then individually packed in opaque black plastic bags.

Due to possible light exposure during sampling, the sediment of both ends of each sample tube was removed in the laboratory under subdued red light (to avoid bleaching of the luminescence signal). The discarded material was then used to estimate the water content and dose rates received during burial. We are confident that sediment grains from the central part of the tubes, which we used to determine  $D_e$ , were not exposed to light during sampling. The samples were dry sieved to separate and remove the  $>500$   $\mu\text{m}$  sediment fraction. The remaining grains were then wet-sieved, and the 90–250  $\mu\text{m}$  fraction extracted and chemically pre-treated by immersing for 96 h in 1 N HCl and 48 h in  $\text{H}_2\text{O}_2$  to eliminate carbonates and organics, respectively. The samples were then sieved again to extract grain sizes in the range 150–250  $\mu\text{m}$ . A K-feldspar enriched extract was then separated using a heavy liquid solution (density  $<2.58$   $\text{g}/\text{cm}^3$ ) and etched for 10 min with 48% HF to remove the outer alpha-irradiated layer from the grains. After etching, any contaminating fluorides were dissolved using HCl. The second stage of dry sieving through a 150  $\mu\text{m}$  sieve was undertaken to obtain the final feldspar concentrate used for experiments. At each stage of the separation procedure, samples were generously rinsed with distilled water. Small ( $\sim 2$  mm) aliquots

**Table A1**  
IRSL Samples, Equivalent Dose, Dose Rate Calculations and Uncorrected Ages Using a Central Age Model

Sample ID	De (Gy)	$\pm$	Depth (m)	$\pm$	Water (%)	$\pm$	K (%)	$\pm$	U (ppm)	$\pm$	Th (ppm)	$\pm$	Cosmic (Gy/ka)	$\pm$	Total (Gy/ka)	$\pm$	Age (ka)	$\pm$
Kashmar 1	335.31	15.95	0.35	0.05	5	2	2.57	$\pm 0.03$	1.98	$\pm 0.10$	9.47	$\pm 0.16$	0.257	0.100	4.15	0.15	80.81	5.4
Kashmar 2	268.42	12.54	0.3	0.05	5	2	2.20	$\pm 0.05$	1.92	$\pm 0.10$	7.45	$\pm 0.21$	0.264	0.100	3.67	0.14	73.15	5.0
Kashmar 3	66.38	2.00	6	0.05	5	2	1.64	$\pm 0.03$	2.03	$\pm 0.10$	8.22	$\pm 0.16$	0.113	0.100	3.08	0.13	21.53	1.3
Kashmar 4	47.25	1.46	4	0.05	5	2	1.55	$\pm 0.05$	1.90	$\pm 0.10$	7.35	$\pm 0.21$	0.143	0.100	2.94	0.13	16.09	1.0
Kashmar 5	328.88	20.38	0.25	0.05	5	2	2.07	$\pm 0.03$	2.04	$\pm 0.10$	8.07	$\pm 0.16$	0.268	0.100	3.62	0.14	90.78	7.1
Kashmar 6	368.66	25.09	0.4	0.05	5	2	2.27	$\pm 0.05$	2.28	$\pm 0.10$	8.91	$\pm 0.21$	0.248	0.100	3.90	0.15	94.60	7.9
Kashmar 8	273.33	13.73	0.75	0.05	5	2	2.44	$\pm 0.05$	2.33	$\pm 0.10$	9.39	$\pm 0.21$	0.217	0.100	4.07	0.15	67.21	4.6
Kashmar 9	270.42	11.07	0.75	0.05	5	2	2.44	$\pm 0.03$	2.32	$\pm 0.10$	9.13	$\pm 0.16$	0.217	0.100	4.04	0.15	66.88	4.2
Kashmar 10	196.96	18.81	3	0.05	5	2	2.04	$\pm 0.05$	1.45	$\pm 1.54$	5.13	$\pm 1.13$	0.163	0.100	3.15	0.29	62.46	8.5
Kashmar 11	190.93	13.64	3	0.05	5	2	2.14	$\pm 0.03$	1.17	$\pm 0.83$	3.89	$\pm 0.84$	0.163	0.100	3.10	0.19	61.61	6.1
Kashmar 12A	197.80	18.15	4	0.05	5	2	2.46	$\pm 0.05$	1.66	$\pm 0.77$	5.30	$\pm 0.76$	0.143	0.100	3.58	0.20	55.22	6.1
Kashmar 12b	201.67	11.56	4	0.05	5	2	2.46	$\pm 0.05$	1.66	$\pm 0.77$	5.30	$\pm 0.76$	0.143	0.100	3.58	0.20	56.30	4.8

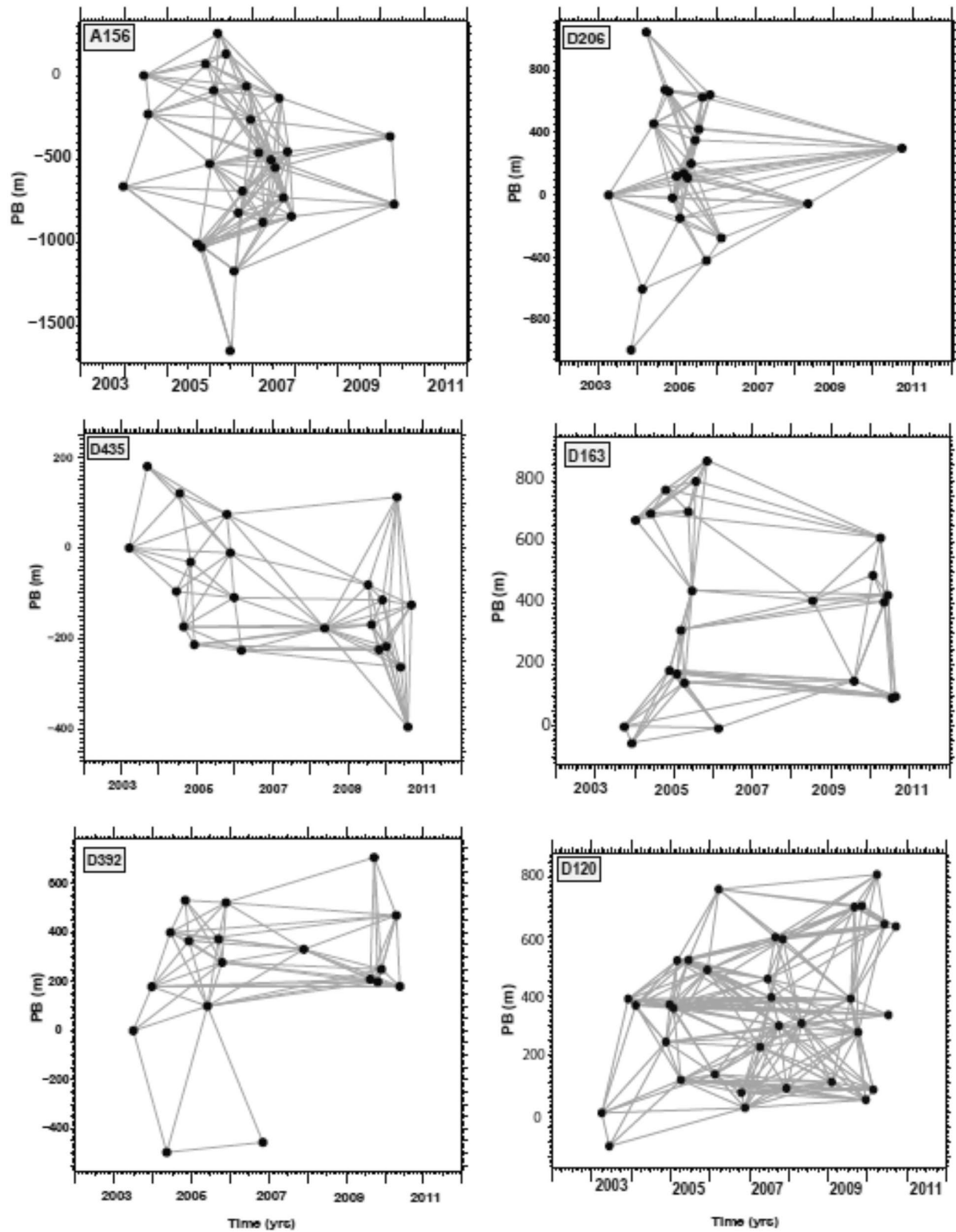


**Figure A1.** Diagram showing the network of processed interferograms (gray lines) for each of the six tracks used in this study (five descending and one ascending). Each plot shows the relative perpendicular baselines as a function of acquisition dates. Each date of ENVISAT image acquisition is represented by a black dot.

were mounted on 10-mm diameter aluminum discs using silicone oil as an adhesive for the single-aliquot analyses.

All the experiments reported here were conducted using a Risø TL-DA-15 system, equipped with an infrared light diode emitting at 830 nm and a blue light diode array ( $\lambda = 470$  nm,  $p = 24$  mW cm<sup>-2</sup>) as stimulation sources. IRSL signals were detected using an EMI-9235QA photomultiplier tube and measured through the Schott 2 mm thick BG39 and Corning 4 mm thick 7–59 filters (blue emission). Samples were irradiated using standard sealed <sup>90</sup>Sr/<sup>90</sup>Y beta sources, calibrated against known  $\gamma$ -irradiated samples over a range of grain sizes from 5 to 200  $\mu$ m (Armitage & Bailey, 2005).

For age determination, we followed the approaches used by Fattahi et al. (2007). The dose rates for each sample were calculated using radioisotope concentrations, present-day moisture content, and burial depths. Uranium, thorium, and potassium concentrations were measured with ICP mass spectrometry (Table A1). Present-day moisture contents were estimated by drying at 40 °C. Moisture contents obtained directly from the samples were generally low, and spread from 0.2% to 6.7%. For our calculations, we considered  $2 \pm 2\%$  moisture contents for all samples. We use the conversion factors of Adamiec and Aitken (1998) and Aitken (1985) to calculate the resulting alpha, beta, and gamma dose rates. Alpha and beta dose rates were corrected for attenuation due to grain size using the factors of Bell (1980) and Mejdahl (1979). An alpha efficiency of  $0.04 \pm 0.02$  was assumed for all quartz samples. Cosmic-ray dose rates were calculated from burial depth and overburden density (1.85 g cm<sup>-3</sup>) using the formula given by Prescott and Hutton (1988). For feldspar dose rate calculations, an internal potassium content of  $12.5 \pm 0.5\%$  and an  $a$ -value of  $0.150 \pm 0.015$  were assumed, for feldspar samples following Preusser (2003). Table A1 shows the values used to determine the annual dose rates, along with ages uncorrected for fading.

We tested for fading on the feldspar signals using methods as described in Fattahi et al. (2007). The measured  $g$ -values are variable between samples from the same catchments, from individual geomorphic surfaces, and even from samples extracted from the same sample pits. Applying fading corrections for each individual sample increases the spread of sample ages within each site with respect to the ages uncorrected for fading, suggesting to us that, on average, the fading is on average similar for samples measured using the same approach within each individual catchment.

To account for the fading present within each sample, but without introducing wide scattering of individual sample ages within age geomorphic surface, we calculated the average  $g$ -value for each site (A, B, and C) and then determined the standard error on the three site averages using the sample standard deviation divided by the square root of the number of observations. This gives a first-order estimate of the mean fading value, and the uncertainty attached to it. For each site, we estimated the fading correction at the higher 1 sigma fading limit (from the standard error added to the mean fading value for that catchment), and used this to estimate a fractional uncertainty introduced from the uncertainty on the  $g$ -value. This uncertainty is nonsymmetrical, and we were conservative in using the larger high-side (in age) 1 sigma limit to estimate the fractional error from fading.

We then corrected each of the ages within the three individual catchments using our estimated correction factor. We added the estimated uncertainty contribution in quadrature to the scaled (corrected) age uncertainty to get a combined corrected age uncertainty, which takes account of the IRSL measurement uncertainties (the regular error estimate) and the fading uncertainty (judged from the degree of variation within that catchment). All values used for calculating fading corrections, along with the final corrected ages are shown in Table A2. The final corrected ages are also summarized in Table 1 in the main text.

## A2. Uranium-Series Dating

Four individual pebbles (KASH A-D) were collected from the sample pit at a depth of  $\sim 55$  cm. The pebbles were selected for the integrity and thickness of carbonate growth. The carbonate rind of KASH-A was lost on slicing the pebble and KASH-D did not provide thick enough carbonate growth from which to derive a microstratigraphy. The two remaining samples (KASH-B and KASH-C) were used for dating.

On slicing the two successful samples, a clear microstratigraphy was seen within the carbonate, and mapped under magnification. The mapped stratigraphy within the rinds shows discrete periods of growth,

Tropospheric delay map for track D392

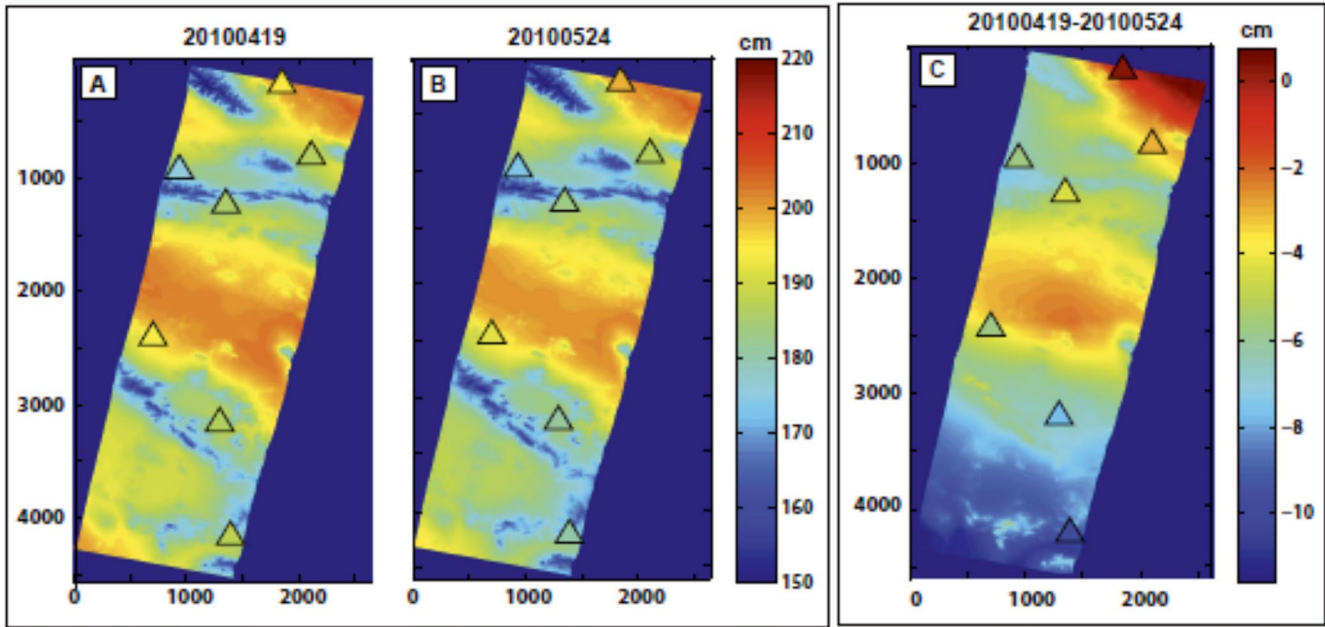


**Figure A2.** The tropospheric delay map estimated by ERA-I (for track D392). (a and b) The delay map for dates 20100419 and 20100524, respectively. The triangles show the GPS stations, with the color of the triangles representing the value of GPS tropospheric delay according to color bar, taken at the SAR image date. (c) The delay map for 1-month interferogram (20100419–20100524).

**Table A2**

*Fading Corrections and Final Age. The Table is Arranged by Each Individual Catchment (Sites A, B, and C). G-values are Given for Each Sample Null Ages of Each Corrected Using Those G-values*

Site	Raw ka	± 1 sigma	g-value	Corr age	± 1 sigma	Corr Ratio	Mean g-value	Mean corr factor	corr age	orig error	Frac err	new frac err	new err
Site 1													
#10	62.5	8.5	4.0	93.0	12.4	1.5			70.7	9.6	0.14	0.20	14.17
#11	61.6	6.1	1.6	71.2	7.0	1.2			69.7	6.9	0.10	0.18	12.37
#12a	55.2	6.1	-1.0	55.2	5.9	1.0			62.5	6.9	0.11	0.18	11.5
#12b	56.3	4.8	fading	not	measured				63.7	5.4	0.09	0.17	10.8
	mean g-value	1.5					1.5 +/- 1.4	1.13					
Eddi	stdev	2.5					mean correction Ratio	1.21					
	std err	1.4					stdev	0.249855					
							std err	0.083285					
Site 2													
#5	90.8	7.1	fading	not	measured				130.9	10.2	0.08	0.10	13.00
#6	94.6	7.9	3.1	127.8	10.5	1.4			136.4	11.4	0.08	0.10	14.12
#8	67.2	4.6	4.7	108.6	7.1	1.6			96.9	6.6	0.07	0.09	8.9
#9	66.9	4.2	4.0	99.7	6.1	1.5			96.4	6.1	0.06	0.09	8.5
	mean	3.9					3.9 +/- 0.5	1.44					
	stdev	0.8					mean correction Ratio	1.49					
	std err	0.5					stdev	0.132282					
							std err	0.044094					
Site 3													
#1	80.8	5.4	2.4	101.2	6.4	1.3			98.6	6.6	0.07	0.08	7.3
#2	73.2	5.0	1.8	86.4	5.5	1.2			89.2	6.1	0.07	0.08	6.8
#3	21.5	1.3	3.2	28.9	1.7	1.3			26.3	1.6	0.06	0.07	1.8
#4	16.1	1.0	2.0	19.3	1.1	1.2			19.6	1.2	0.06	0.07	1.4
	mean	2.3					2.3 +/- 0.3	1.22					
	stdev	0.6					mean correction Ratio	1.24					
	std err	0.3				1.3	stdev	0.072421					
							std err	0.02414					

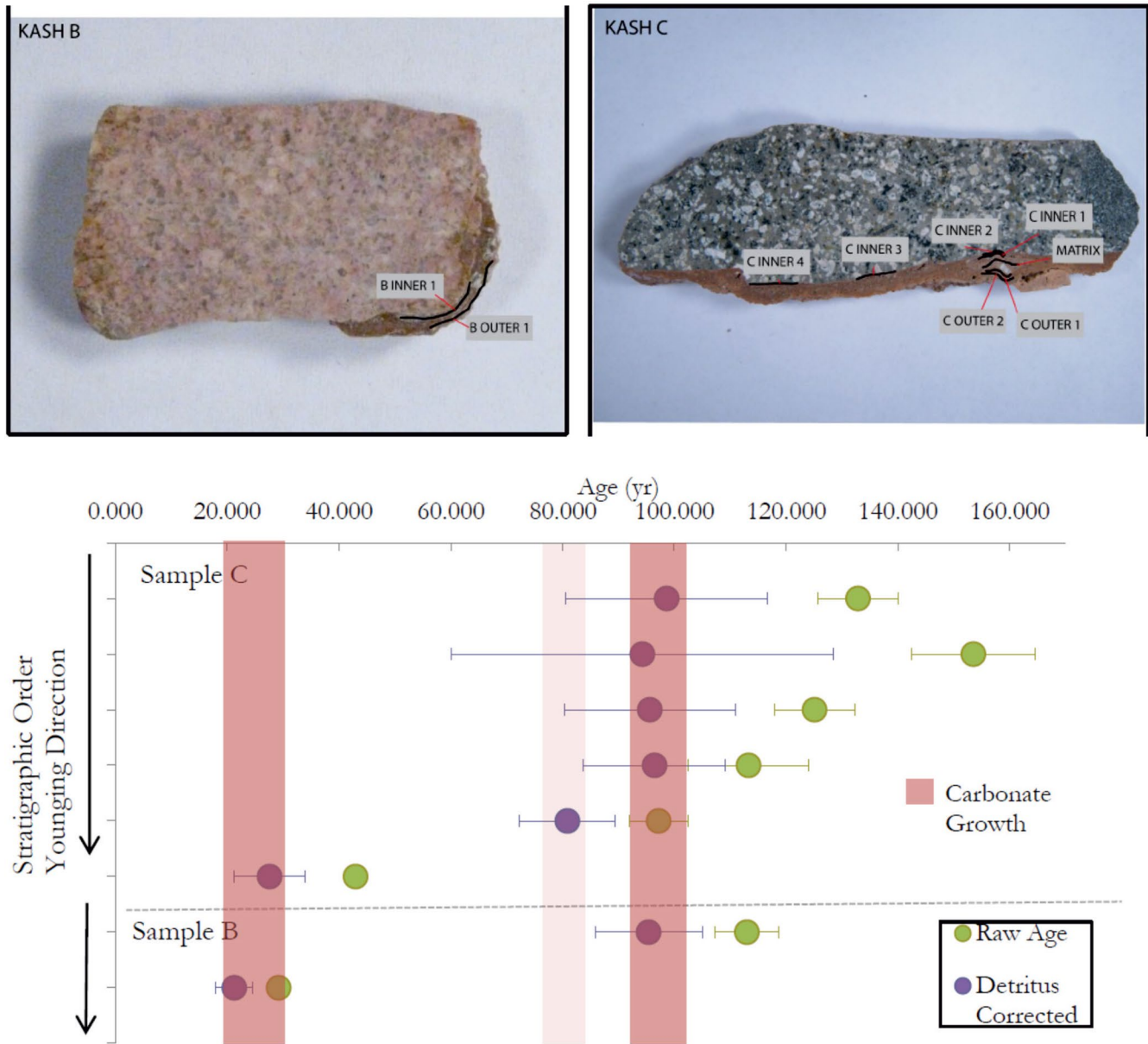


**Figure A3.** (a and b) Photographs of the two pebble rinds that were sampled for U-series dating. Sub-samples from individual growth layers are labeled. (b) Raw and detritally corrected ages from the two samples. Five samples lie on an isochron and hence appear to be co-eval, with an isochron-derived age of  $95.23 \pm 2.76$  ka for this period of growth. Corrected ages also define periods of growth  $\sim 80$  ka (one sample) and  $\sim 20$ – $30$  ka (two samples).

characterized by different textures and by the degree to which detrital material has been incorporated. Patches of irregular growth within the rinds (particularly for KASH-C) were mapped and avoided during sampling, as we consider these to be inclusions that have been incorporated within the rind.

Seven samples were taken from KASH-C and two from KASH-B (Figure A3). These samples were taken from the cleanest section of each growth layer. The innermost layer of KASH-C was sampled twice (labeled C Inner 3, C Inner 4) as this layer represents the earliest onset of carbonate growth, and so the most important for our overall study aims. To target thin ( $<1$  mm) carbonate growths, we used a New Wave micromill drill. The pebble slice was attached to the stage and a microscope image was used to trace out the path of the microdrill. Slow drill speed, plunge speed, and scan speed were used to minimize the loss of material when drilling. The powder was then collected with a scalpel and weighed. Between each sample collection,

**Table A3**  
Uranium Concentrations, U-Series Ratios, and Uncorrected Ages Calculated Using the Procedures Outlines in A2

Subsample ID	<sup>238</sup> U conc. (ppm)	<sup>230</sup> Th/ <sup>238</sup> U	<sup>232</sup> Th/ <sup>238</sup> U	<sup>234</sup> U/ <sup>238</sup> U	Uncorrected age (kyr)	Age uncertainty
C Outer 1	1.52	0.7636 ± 0.0369	0.1695 ± 0.0043	1.2624 ± 0.0145	96,763	+7,728–5,764
C Outer 2	5.41	0.4255 ± 0.0171	0.1620 ± 0.0039	1.2933 ± 0.0137	42,698	+6,045–7,254
C Inner 1	0.97	0.8391 ± 0.0583	0.1773 ± 0.0076	1.2566 ± 0.0208	113,607	+5,429–5,198
C Inner 2	3.63	0.8879 ± 0.0365	0.2925 ± 0.0074	1.2590 ± 0.0142	124,839	+12,513–11,359
C Inner 3	4.45	0.9462 ± 0.0476	0.4964 ± 0.0126	1.2118 ± 0.0134	153,232	+19,934–17,135
C Inner 4	4.82	0.8945 ± 0.0460	0.3238 ± 0.0075	1.2309 ± 0.0128	132,537	+27,188–22,130
C Matrix	2.66	1.0092 ± 0.0420	0.6050 ± 0.0159	1.2448 ± 0.0134	164,489	+13,939–12,572
B Outer 1	5.57	0.3070 ± 0.0158	0.0865 ± 0.0020	1.3006 ± 0.0144	28,967	+13,079–11,771
B Outer 2	4.10	0.8247 ± 0.0431	0.1800 ± 0.0042	1.2428 ± 0.0129	112,671	+21,189–17,983

the drill and pebble slice were thoroughly cleaned with compressed air to ensure no cross-contamination of powder.

Uranium and Thorium were separated and their isotopic ratios were measured with a Nu Plasma multi-collector inductively coupled plasma mass spectrometer (MC ICP-MS), following the same methods and processes as described in Gregory et al. (2014). Uranium concentrations, U-series isotope ratios, and ages calculated using the equation of Broecker (1963) are listed in Table A3. To correct for the effect of detrital contamination on the calculated ages, we first determined detrital composition by assuming a crustal elemental abundance of Uranium and Thorium archived in the EarthChem database (<http://www.earthchem.org>), and then derived a <sup>230</sup>Th/<sup>238</sup>U ratio of 0.7607 ± 0.0139 and a <sup>234</sup>U/<sup>238</sup>U ratio of 1.2679 ± 0.172 from the isochron relationship (e.g., Bischoff & Fitzpatrick, 1991; Luo & Ku, 1991) using the four “C-Inner” samples and “B-Outer-2” (Table A3). To constrain the uncertainty of detrital isotopic concentration, the isochron slopes and intercepts were calculated using a York fit, with error weighted in both *x* and *y*. The resulting isochron age for carbonate growth is 95.2 ± 2.76 ka.

#### Acknowledgments

The authors thank the European Space Agency (ESA) for providing Envisat SAR images and IKONOS imagery through CAT-1 projects 6462 and 7023. The authors are grateful to JPL/Caltech for use of the ROI\_PAC software. The authors thank the Geological Survey of Iran for their continued support of our work. Mr. Hosseini of the Kerman office of the Geological Survey and Mr. Soltani of the International Research and Collaboration Office of the Iranian Ministry of Education were both extremely kind in helping with the logistics of the project. Hussain Beni-Asadi is thanked for his safe and patient driving in the field. The study was funded by the Royal Society of London through a University Research Fellowship awarded to Richard T. Walker and by Research Grants from the Leverhulme Trust (ACRNUB0 and EROICA – RPG-2018-371). The authors also acknowledge UK Research Council support through the NERC-ESRC Earthquakes without Frontiers consortium (EwF\_NE/J02001X/1\_1), COMET (GA/13/M/031), and allocation 0009090 from the Research England GCRF Support Fund.

#### Data Availability Statement

Maps were prepared using Generic Mapping Tools software (Wessel & Smith, 1995). FAIR data access statement: For the interferometry, we used Envisat data, which was originally obtained through a European Space Agency Category 1 project (7023), and which is now archived and freely available through the ESA online catalog ([http://esar-ds.eo.esa.int/socat/SAR-ASA\\_IMS\\_1P/pair\\_search](http://esar-ds.eo.esa.int/socat/SAR-ASA_IMS_1P/pair_search)). Commercial Quickbird satellite imagery used within this analysis was obtained at no cost through ESA Category 1 project (6462). The data were obtained under license and are available for purchase from Maxar (<https://www.maxar.com/>). All data derived from IRSL and U-series dating are provided in full within the main body of the study.

#### References

- Adamiec, G., & Aitken, M. (1998). Dose rate conversion factors: Update. *Ancient Thermoluminescence*, 16, 37–49.
- Aitken, M. (1985). *Thermoluminescence dating*. Academic Press.
- Ambraseys, N. N., & Melville, C. P. (1982). *A history of Persian earthquakes*. Cambridge University Press.
- Armitage, S. J., & Bailey, R. M. (2005). The measured dependence of laboratory beta dose rates on sample grain size. *Radiation Measurements*, 39, 123–127. <https://doi.org/10.1016/j.radmeas.2004.06.008>
- Baker, C., (1993). *The active seismicity and tectonics of Iran* (Doctoral dissertation). University of Cambridge.
- Bell, W. T. (1980). Alpha dose attenuation in quartz grains for thermoluminescence dating. *Ancient Thermoluminescence*, 12, 4–8. <https://doi.org/10.1097/01376517-198009000-00001>
- Berardino, P., Fornaro, G., Lanari, R., & Sansosti, E. (2002). A new algorithm for surface deformation monitoring based on small baseline differential SAR interferograms. *IEEE Transactions Geoscience Remote Sensing*, 40(11), 2375–2383. <https://doi.org/10.1109/tgrs.2002.803792>
- Berberian, M. (1976). *Contribution to the seismotectonics of Iran (Part II)*. Report no. 39. Geological Survey of Iran.

- Berrada Baby, H., Golé, P., & Lavernat, J. (1988). A model for the tropospheric excess path length of radio waves from surface meteorological measurements. *Radio Science*, 23(6), 1023. <https://doi.org/10.1029/rs023i006p01023>
- Bischoff, J. L., & Fitzpatrick, J. A. (1991). U-series dating of impure carbonates: An isochron technique using total-sample dissolution. *Geochimica et Cosmochimica Acta*, 55(2), 543–554. [https://doi.org/10.1016/0016-7037\(91\)90011-s](https://doi.org/10.1016/0016-7037(91)90011-s)
- Broecker, W. S. (1963). A preliminary evaluation of uranium series in equilibrium as a tool for absolute age measurement on marine carbonates. *Journal of Geophysical Research*, 68(9), 2817–2834. <https://doi.org/10.1029/jz068i009p02817>
- Cavalié, O., Doin, M.-P., Lasserre, C., & Briole, P. (2007). Ground motion measurement in the Lake Mead area, Nevada, by differential synthetic aperture radar interferometry time series analysis: Probing the lithosphere rheological structure. *Journal of Geophysical Research*, 112(B3), B03403. <https://doi.org/10.1029/2006jb004344>
- Copley, A. (2008). Kinematics and dynamics of the southeastern margin of the Tibetan Plateau. *Geophysical Journal International*, 174(3), 1081–1100. <https://doi.org/10.1111/j.1365-246x.2008.03853.x>
- Cowgill, E. (2007). Impact of riser reconstructions on estimation of secular variation in rates of strike-slip faulting: Revisiting the Charchen River site along the Altyn Tagh Fault, NW China. *Earth and Planetary Science Letters*, 254, 239–255. <https://doi.org/10.1016/j.epsl.2006.09.015>
- Djamour, Y., Vernant, P., Nankali, H. R., & Tavakoli, F. (2011). NW Iran-eastern Turkey present-day kinematics: Results from the Iranian permanent GPS network. *Earth and Planetary Science Letters*, 307(1–2), 27–34. <https://doi.org/10.1016/j.epsl.2011.04.029>
- Doin, M.-P., Guillaso, S., Jolivet, R., Lasserre, C., Lodge, F., Ducret, G., & Grandin, R. (2011). Presentation of the small-baseline NSBAS processing chain on a case example: The ETNA deformation monitoring from 2003 to 2010 using ENVISAT data. Paper presented at European Space Agency Symposium Fringe, September 19–23, 2011, pp. 303–304.
- Doin, M. P., Lasserre, C., Peltzer, G., Cavalié, O., & Doubre, C. (2009). Corrections of stratified tropospheric delays in SAR interferometry: Validation with global atmospheric models. *Journal of Applied Geophysics*, 69(1), 35. <https://doi.org/10.1016/j.jappgeo.2009.03.010>
- Ducret, G., Doin, M. P., Grandin, R., Lasserre, C., & Guillaso, S. (2013). Dem corrections before unwrapping in a small baseline strategy for InSAR time series analysis. *IEEE Geoscience and Remote Sensing Letters*, 11(3), 696–700.
- Engdahl, E. R., Jackson, J. A., Myers, S. C., Bergman, E. A., & Priestley, K. (2006). Relocation and assessment of seismicity in the Iran region. *Geophysical Journal International*, 167(2), 761–778.
- Engdahl, E. R., van der Hilst, R., & Buland, R. (1998). Global teleseismic earthquake relocation with improved travel times and procedures for depth determination. *Bulletin of the Seismological Society of America*, 88(3), 722–743.
- Farbod, Y., Bellier, O., Shabanian, E., & Abbassi, M. R. (2011). Geomorphic and structural variations along the Doruneh Fault System (Central Iran). *Tectonics*, 30(6). <https://doi.org/10.1029/2011tc002889>
- Farbod, Y., Shabanian, E., Bellier, O., Abbassi, M. R., Braucher, R., Benedetti, L., et al. (2016). Spatial variations in late Quaternary slip rates along the Doruneh Fault System (Central Iran). *Tectonics*, 35(2), 386–406. <https://doi.org/10.1002/2015tc003862>
- Farr, T. G., Rosen, P. A., Caro, E., Crippen, R., Duren, R., Hensley, S., et al. (2007). The shuttle radar topography mission. *Reviews of Geophysics*, 45(2). <https://doi.org/10.1029/2005rg000183>
- Fattahi, M., & Walker, R. (2006). Luminescence dating of the last earthquake of the Sabzevar thrust fault, NE Iran. *Quaternary Geochronology*, 2, 284–328.
- Fattahi, M., Walker, R. T., Khatib, M. M., Dolati, A., & Bahroudi, A. (2007). Slip-rate estimate and past earthquakes on the Doruneh fault, Eastern Iran. *Geophysical Journal International*, 168, 691–709. <https://doi.org/10.1111/j.1365-246x.2006.03248.x>
- Fattahi, M., Walker, R. T., Talebian, M., Sloan, R. A., & Rasheedi, A. (2014). Late Quaternary active faulting and landscape evolution in relation to the Gowk Fault in the South Golbaf Basin, S.E. Iran. *Geomorphology*, 204, 334–343. <https://doi.org/10.1016/j.geomorph.2013.08.017>
- Foroutan, M., Meyer, B., Sébrier, M., Nazari, H., Murray, A. S., Le Dortz, K., et al. (2014). Late Pleistocene-Holocene right slip rate and paleoseismology of the Nayband fault, western margin of the Lut block, Iran. *Journal Geophysical Research: Solid Earth*, 119(4), 3517–3560. <https://doi.org/10.1002/2013jb010746>
- Giessner, K., Hagedorn, H., & Sarvati, M. R. (1984). Geomorphological studies in the Kashmir region (NE Iran). *Neues Jahrbuch für Geologie und Paläontologie*, 168, 545–557. <https://doi.org/10.1127/njgpa/168/1984/545>
- Goldstein, R. M., & Werner, C. L. (1998). Radar interferogram filtering for geophysical applications. *Geophysical Research Letters*, 25(21), 4035–4038. <https://doi.org/10.1029/1998gl900033>
- Goldstein, R. M., Zebker, H. A., & Werner, C. L. (1988). Satellite radar interferometry: Two-dimensional phase unwrapping. *Radio Science*, 23(4), 713–720. <https://doi.org/10.1029/rs023i004p00713>
- Gregory, L. C., Thomas, A. L., Walker, R. T., Garland, R., Mac Niocaill, C., Fenton, C. R., et al. (2014). Combined uranium series and <sup>10</sup>Be cosmogenic exposure dating of surface abandonment: A case study from the Ölgüy strike-slip fault in western Mongolia. *Quaternary Geochronology*, 24, 27–43. <https://doi.org/10.1016/j.quageo.2014.07.005>
- Hooper, A., Segall, P., & Zebker, H. (2007). Persistent scatterer interferometric synthetic aperture radar for crustal deformation analysis, with application to Volcán Alcedo, Galápagos. *Journal of Geophysical Research: Solid Earth*, 112(B7). <https://doi.org/10.1029/2006jb004763>
- Jackson, J., & McKenzie, D. (1984). Active tectonics of the Alpine-Himalayan Belt between western Turkey and Pakistan. *Geophysical Journal International*, 77(1), 185. <https://doi.org/10.1111/j.1365-246x.1984.tb01931.x>
- Jolivet, R., Grandin, R., Lasserre, C., Doin, M.-P., & Peltzer, G. (2011). Systematic InSAR tropospheric phase delay corrections from global meteorological reanalysis data. *Geophysical Research Letters*, 38(17). <https://doi.org/10.1029/2011gl048757>
- Luo, S., & Ku, T.-L. (1991). U-series isochron dating: A generalized method employing total-sample dissolution. *Geochimica et Cosmochimica Acta*, 55(2), 555–564. [https://doi.org/10.1016/0016-7037\(91\)90012-t](https://doi.org/10.1016/0016-7037(91)90012-t)
- Massonnet, D., & Feigl, K. L. (1998). Radar interferometry and its application to changes in the earth's surface. *Reviews of Geophysics*, 36(4), 441–500. <https://doi.org/10.1029/97rg03139>
- Mattei, M., Cifelli, F., Alimohammadian, H., Rashid, H., Winkler, A., & Sagnotti, L. (2017). Oroclinal bending in the Alborz Mountains (Northern Iran): New constraints on the age of South Caspian subduction and extrusion tectonics. *Gondwana Research*, 42, 13–28. <https://doi.org/10.1016/j.gr.2016.10.003>
- McKenzie, D. (1972). Active tectonics of the Mediterranean region. *Geophysical Journal International*, 30(2), 109–185. <https://doi.org/10.1111/j.1365-246x.1972.tb02351.x>
- Mejdahl, V. (1979). Thermoluminescence dating: Beta-dose attenuation in quartz grains. *Archaeometry*, 21, 61–72. <https://doi.org/10.1111/j.1475-4754.1979.tb00241.x>
- Mousavi, Z., Pathier, E., Walker, R. T., Walpersdorf, A., Tavakoli, F., Nankali, H., et al. (2015). Interseismic deformation of the Shahroud fault system (NE Iran) from space-borne radar interferometry measurements. *Geophysical Research Letters*, 42(14), 5753–5761. <https://doi.org/10.1002/2015gl064440>

- Mousavi, Z., Walpersdorf, A., Walker, R. T., Tavakoli, F., Pathier, E., Nankali, H., et al. (2013). Global Positioning System constraints on the active tectonics of NE Iran and the South Caspian region. *Earth and Planetary Science Letters*, 377–378, 287–298. <https://doi.org/10.1016/j.epsl.2013.07.007>
- Pezzo, G., Tolomei, C., Atzori, S., Salvi, S., Shabanian, E., Bellier, O., & Farbod, Y. (2012). New kinematic constraints of the Western Doruneh fault, Northeastern Iran, from interseismic deformation analysis. *Geophysical Journal International*, 190(1), 622. <https://doi.org/10.1111/j.1365-246x.2012.05509.x>
- Prescott, J. R., & Hutton, J. T. (1988). Cosmic ray and gamma ray dosimetry for TL and ESR. *International Journal of Radiation Applications and Instrumentation - Part D: Nuclear Tracks and Radiation Measurements*, 14, 223–227. [https://doi.org/10.1016/1359-0189\(88\)90069-6](https://doi.org/10.1016/1359-0189(88)90069-6)
- Preusser, F. (2003). IRSL dating of K-rich feldspars using the SAR protocol: Comparison with independent age control. *Ancient Thermoluminescence*, 21, 17–23.
- Regard, V., Bellier, O., Braucher, R., Gasse, F., Bourles, D., Mercier, J., et al. (2005). <sup>10</sup>Be dating of alluvial deposits from Southeastern Iran (the Hormoz Strait area). *Palaeogeography, Paleoclimatology, Palaeoecology*, 242, 36–53.
- Ritz, J. F., Balescu, S., Soleymani, S., Abbassi, M., Nazari, H., Feghhi, K., et al. (2003). Determining the long-term slip rate along the Mosha Fault, Central Alborz, Iran. Implications in terms of seismic activity. Paper presented at Proceeding of the 4th International Conference on Seismology and Earthquake Engineering (Vol. 1214).
- Rizza, M., Mahan, S., Ritz, J. F., Nazari, H., Hollingsworth, J., & Salamati, R. (2011). Using luminescence dating of coarse matrix material to estimate the slip rate of the Astaneh fault, Iran. *Quaternary Geochronology*, 6(3–4), 390–406. <https://doi.org/10.1016/j.quageo.2011.03.001>
- Rizza, M., Vernant, P., Ritz, J. F., Peyret, M., Nankali, H., Nazari, H., et al. (2013). Morphotectonic and geodetic evidence for a constant slip-rate over the last 45 kyr along the Tabriz fault (Iran). *Geophysical Journal International*, 193(3), 1083–1094. <https://doi.org/10.1093/gji/ggt041>
- Rosen, P. A., Hensley, S., Peltzer, G., & Simons, M. (2004). Updated repeat orbit interferometry package released. *Eos, Transactions American Geophysical Union*, 85(5), 47. <https://doi.org/10.1029/2004eo050004>
- Schmidt, D. A., & Bürgmann, R. (2003). Time-dependent land uplift and subsidence in the Santa Clara valley, California, from a large interferometric synthetic aperture radar data set. *Journal of Geophysical Research*, 108(B9). <https://doi.org/10.1029/2002jb002267>
- Shabanian, E., Siame, L., Bellier, O., Benedetti, L., & Abbassi, M. R. (2009). Quaternary slip rates along the northeastern boundary of the Arabia-Eurasia collision zone (Kopeh Dagh Mountains, Northeast Iran). *Geophysical Journal International*, 178(2), 1055–1077. <https://doi.org/10.1111/j.1365-246x.2009.04183.x>
- Talebian, M., Copley, A. C., Fattahi, M., Ghorashi, M., Jackson, J. A., Nazari, H., et al. (2016). Active faulting within a megacity: The geometry and slip rate of the Pardisan thrust in Central Tehran, Iran. *Geophysical Journal International*, 207(3), 1688–1699. <https://doi.org/10.1093/gji/ggw347>
- Tavakoli, F. (2007). *Present-day deformation and kinematics of the active faults observed by GPS in the Zagros and east of Iran* (Unpublished Ph.D. Thesis). Université Joseph-Fourier.
- Tavakoli, F., Walpersdorf, A., Authemayou, C., Nankali, H. R., Hatzfeld, D., Tatar, M., et al. (2008). Distribution of the right-lateral strike-slip motion from the Main Recent Fault to the Kazerun Fault System (Zagros, Iran): Evidence from present-day GPS velocities. *Earth and Planetary Science Letters*, 275(3–4), 342–347. <https://doi.org/10.1016/j.epsl.2008.08.030>
- Tchalenko, J. S., Berberian, M., & Behzadi, H. (1973). Geomorphic and seismic evidence for recent activity on the Doruneh Fault, Iran. *Tectonophysics*, 19(4), 333–341. [https://doi.org/10.1016/0040-1951\(73\)90027-9](https://doi.org/10.1016/0040-1951(73)90027-9)
- Van Der Woerd, J., Tapponnier, P., Ryerson, F. J. F., Meyer, B., Gaudemer, Y., et al. (2002). Uniform postglacial slip-rate along the central 600 km of the Kunlun Fault (Tibet), from <sup>26</sup>Al, <sup>10</sup>Be, and <sup>14</sup>C dating of riser offsets, and climatic origin of the regional morphology. *Geophysical Journal International*, 148(3), 356–388. <https://doi.org/10.1046/j.1365-246x.2002.01556.x>
- Vernant, P., Nilforoushan, F., Hatzfeld, D., Abbassi, M. R., Vigny, C., Masson, F., et al. (2004). Present-day crustal deformation and plate kinematics in the Middle East constrained by GPS measurements in Iran and northern Oman. *Geophysical Journal International*, 157, 381–398. <https://doi.org/10.1111/j.1365-246x.2004.02222.x>
- Walker, R., & Jackson, J. (2004). Active tectonics and late Cenozoic strain distribution in central and Eastern Iran. *Tectonics*, 23, <https://doi.org/10.1029/2003TC001529>
- Walker, R. T., & Fattahi, M. (2011). A framework of Holocene and Late Pleistocene environmental change in eastern Iran inferred from the dating of periods of alluvial fan abandonment, river terracing, and lake deposition. *Quaternary Science Reviews*, 30, 1256–1271. <https://doi.org/10.1016/j.quascirev.2011.03.004>
- Walker, R. T., Talebian, M., Sloan, R. A., Rasheedi, A., Fattahi, M., & Bryant, C. (2010). Holocene slip-rate on the Gowk strike-slip fault and implications for the distribution of tectonic strain in eastern Iran. *Geophysical Journal International*, 181(1), 221–228. <https://doi.org/10.1111/j.1365-246x.2010.04538.x>
- Walpersdorf, A., Hatzfeld, D., Nankali, H., Tavakoli, F., Nilforoushan, F., Tatar, M., et al. (2006). Difference in the GPS deformation pattern of North and Central Zagros (Iran). *Geophysical Journal International*, 167(3), 1077–1088. <https://doi.org/10.1111/j.1365-246x.2006.03147.x>
- Walpersdorf, A., Manighetti, I., Mousavi, Z., Tavakoli, F., Vergnolle, M., Jadidi, A., et al. (2014). Present-day kinematics and fault slip rates in eastern Iran, derived from 11 years of GPS data. *Journal of Geophysical Research: Solid Earth*, 119(2), 1359–1383. <https://doi.org/10.1002/2013jb010620>
- Wellman, H. W. (1966). Active wrench faults of Iran, Afghanistan and Pakistan. *Geologische Rundschau*, 55(3), 716–735. <https://doi.org/10.1007/bf02029650>
- Wessel, P., & Smith, W. H. F. (1995). New version of the generic mapping tools. *Eos, Transactions American Geophysical Union*, 76(33), p. 329. <https://doi.org/10.1029/95eo00198>
- Zebker, H. A., Rosen, P. A., & Hensley, S. (1997). Atmospheric effects in interferometric synthetic aperture radar surface deformation and topographic maps. *Journal of Geophysical Research*, 102(B4), 7547–7563. <https://doi.org/10.1029/96jb03804>
- Zebker, H. A., & Villasenor, J. (1992). Decorrelation in interferometric radar echoes. *IEEE Transactions on Geoscience and Remote Sensing*, 30(5), 950–959. <https://doi.org/10.1109/36.175330>